



HAL
open science

Contractional deformation between extensional dome exhumation in Central Pamir at 17–15 Ma constrained by metamorphic and paleomagnetic data from the Bartang volcanic rocks, Tajikistan

Jovid Aminov, Pierrick Roperch, Guillaume Dupont-Nivet, Carole Cordier, Stéphane Guillot, Johannes Glodny, Martin Timmerman, Masafumi Sudo, Gilles Ruffet, Max Wilke, et al.

► To cite this version:

Jovid Aminov, Pierrick Roperch, Guillaume Dupont-Nivet, Carole Cordier, Stéphane Guillot, et al.. Contractional deformation between extensional dome exhumation in Central Pamir at 17–15 Ma constrained by metamorphic and paleomagnetic data from the Bartang volcanic rocks, Tajikistan. *Tectonophysics*, 2023, 868, pp.230080. 10.1016/j.tecto.2023.230080 . insu-04274606

HAL Id: insu-04274606

<https://insu.hal.science/insu-04274606v1>

Submitted on 8 Nov 2023

HAL is a multi-disciplinary open access archive for the deposit and dissemination of scientific research documents, whether they are published or not. The documents may come from teaching and research institutions in France or abroad, or from public or private research centers.

L'archive ouverte pluridisciplinaire **HAL**, est destinée au dépôt et à la diffusion de documents scientifiques de niveau recherche, publiés ou non, émanant des établissements d'enseignement et de recherche français ou étrangers, des laboratoires publics ou privés.

**Contractional deformation between extensional dome exhumation in
Central Pamir at 17-15 Ma constrained by metamorphic and paleomagnetic
data from the Bartang volcanic rocks, Tajikistan**

Jovid Aminov^{1-4*}, Pierrick Roperch², Guillaume Dupont-Nivet^{2,5}, Carole Cordier⁶,
Stéphane Guillot⁶, Johannes Glodny⁷, Martin J. Timmerman⁵, Masafumi Sudo⁵,
Gilles Ruffet², Max Wilke⁵, France Lagroix⁸, Ding Lin¹, Yunus Mamadjanov⁹

*1 Key Laboratory of Continental Collision and Plateau Uplift, Institute of Tibetan Plateau Research,
Chinese Academy of Sciences, Beijing, China.*

2 Géosciences Rennes, CNRS, Univ. Rennes, 35042 Rennes France.

*3 Department of Earth and Environmental Sciences, University of Central Asia, 736000, Khorog,
Tajikistan*

*4 Institute of Geology, Earthquake Engineering and Seismology, National Academy of Sciences of
Tajikistan, Dushanbe 734063, Tajikistan.*

5 Institute of Geosciences, Potsdam University, Potsdam, Germany.

*6 Univ. Grenoble Alpes, Univ. Savoie Mont Blanc, CNRS, IRD, Univ. G. Eifel, ISTerre, 38000 Grenoble,
France.*

7 GFZ German Research Centre for Geosciences, Telegrafenberg, D-14473 Potsdam, Germany.

8 Université Paris Cité, Institut de physique du globe de Paris, CNRS, F-75005 Paris, France.

*9 Research Center for Ecology and Environment of Central Asia (Dushanbe), Dushanbe 734063,
Tajikistan*

*Keywords: Paleomagnetism, Pamir, Volcanic rocks, Metamorphism, Crustal
deformation*

*Correspondent author: Jovid Aminov (jovid.aminov@ucentralasia.org)

Abstract

The debated mechanism and timing of formation of the Pamir orogenic salient provides an ideal case to combine paleomagnetic and metamorphic analyses. Opposing views argue for either oroclinal bending of the Pamir since the India-Asia collision or for an originally arcuate shape, which can be tested using paleomagnetism to estimate vertical-axis rotations. Furthermore, Pamir deformation can be dated and characterized by the analysis of a well-expressed regional metamorphism. However, paleomagnetism is seldom applied to metamorphic rocks such that the significance of their rock magnetic signal with respect to deformation remains poorly understood. We studied a >2 km thick sequence of slightly metamorphosed Cretaceous-Paleogene volcanic and volcanoclastic rocks from the western Central Pamir Mountains using metamorphic petrology, geochronology, and paleomagnetic analyses. These rocks present a medium-grade metamorphism and have undergone fine grained recrystallisation of biotite due to NW-SE compression. $^{40}\text{Ar}/^{39}\text{Ar}$ and Rb/Sr ages (~17 to 15 Ma) on whole rock and biotite, confirm that the greenschist facies metamorphism is related to the coeval exhumation of Pamir gneiss domes during the Middle Miocene. The rocks generally show homogenous magnetic properties. High field magnetic properties and SEM/EDS data show that the main magnetic remanent carrier is titanohematite. Thermal demagnetizations yield complex characteristic remanent magnetization with site-mean directions obtained for only 14 of the 44 studied sites but scattered mainly within the foliation plane defined by the anisotropy of magnetic susceptibility (AMS). These rocks have also unusual magnetic characteristics where strong-field isothermal remanent magnetizations induce an AMS fabric, likely related to the specific composition and structure of the metamorphic titanohematite but independent of the original anisotropy fabrics. Combined paleomagnetic and geochronological data from the Bartang volcanoclastic rocks enable us to identify a ~17–15 Ma compressive deformation event contemporaneous with the emplacement of the gneiss domes and suggest no oroclinal bending since that event.

1. Introduction

The Pamir Orogen is a geologically significant region due to its complex tectonic history. The crust of the Pamirs formed through a series of subduction accretion events during the Mesozoic that assembled terranes originating from Gondwana onto the southern margin of Eurasia

(e.g. Robinson et al., 2015 and references therein). These accreted terranes were then intensely deformed during the India-Asia collision in the Cenozoic (e.g. Rutte et al., 2017b; Stübner et al., 2013b), resulting in the structures we observe today. The thick Pamir crust of up to ~70 km is thought to have formed through crustal thickening in the Mesozoic (e.g. Chapman et al., 2018; Aminov et al., 2017) and early Cenozoic (Rutte et al., 2017b) and the exhumation of gneiss domes since the early Miocene (Rutte et al., 2017b; Stübner et al., 2013b). As Rutte et al. (2017b) showed, gneiss domes in the eastern Pamirs record three deformation phases: 1) late Eocene–early Miocene compression and crustal thickening; 2) early to middle Miocene extensional exhumation of the domes; and 3) late Miocene–Quaternary shortening associated with the collapse of the western Pamir into the Tajik Basin. However, in the western Pamir, the Shakh dara and Alichur dome exhumations continued from 20 to 2 Ma through extension (Stübner et al., 2013b; Worthington et al., 2020).

Extensional structures like gneiss domes form in either syn-collisional or post-collisional (Cordilleran-style domes) settings (Yin, 2004; Whitney et al., 2004). In post-collisional settings, large-scale lithospheric extension induces dome exhumation along bounding extensional shear zones aligned with the regional extension (Coney and Harms, 1984; Tirel et al., 2004; Verdel et al., 2007).

However, in syn-collisional settings like the Pamir, domes are exhumed through extension along shear zones that are not aligned with the regional convergence (e.g., Worthington et al., 2020; Lee et al., 2004), and extension is either parallel (de Sigoyer et al., 2004; Horton et al., 2015) or perpendicular (Laskowski et al., 2017; Murphy et al., 2002; Ratschbacher et al., 1989) to the convergence directions. How the convergence-parallel extension is driven is a question that remains unanswered despite several proposed mechanisms such as lateral extrusion associated with gravitational collapse (Küfner et al., 2018), delamination during indentation (Chapman et al., 2017), oroclinal bending (Imrecke et al., 2019) or a jump of the deformation to the outer zone of the orogen towards the foreland (Searle and Lamont, 2019).

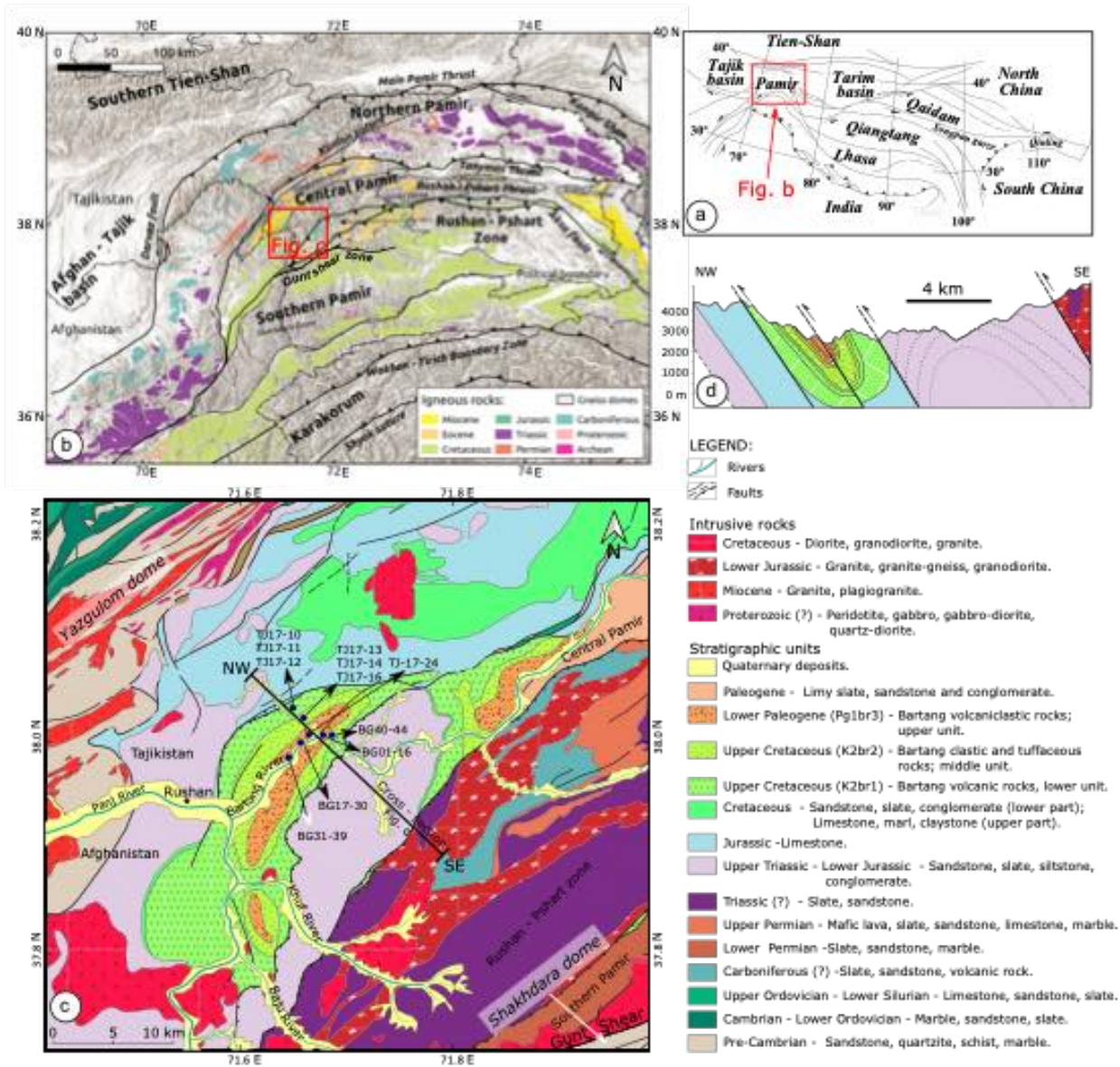


Fig. 1 a) Position of the Pamir orogen within the Tibetan - Himalayan region (modified after Schwab et al., 2004). b) Tectonic map of the Pamir orogen with indication of igneous belts (modified after Aminov et al., 2017; Robinson et al., 2015 and Vlasov et al., 1991). c) Geological map of the Bartang area (modified after Vlasov et al., 1991). Numbers indicate collected samples. Samples with the prefix TJ represent petrologic samples, while those with prefix BG indicate the locations of samples taken for paleomagnetic study. d) NW-SE cross-section across the Bartang volcanoclastic sequence.

The Pamir orogen also forms a northward-convex salient that has been suggested to either form through oroclinal bending and deformation since the early Miocene or be inherited from the Paleozoic accretionary history of the region, including accretion of an oceanic arc in the

Carboniferous (Rembe et al., 2021, 2022) or accretion of Karakum and Tarim in the late Paleozoic (Li et al., 2020a).

In contrast to the Tibetan Plateau, the preserved sediments on the Pamir are heavily deformed and typically metamorphosed. Paleomagnetic studies conducted throughout the Pamir have encountered significant remagnetizations, making it challenging to draw conclusive findings regarding tectonic rotations and their timing (Bazhenov et al., 1996; Waldhör et al., 2001). Building upon these initial investigations, we aim to investigate potential correlations between rock magnetic properties, metamorphism, and deformation in order to evaluate the tectonic implications of paleomagnetic data in metamorphosed rocks within the Pamir region. We chose to study a thick Cretaceous-Paleogene basin filled with lavas and volcanoclastic sediments in the Bartang valley of the western part of the Central Pamir. Because of their location on the western limb of the arc, these rocks can be expected to have been involved in a strong counterclockwise rotation in case of oroclinal bending after their deposition and/or remagnetization and metamorphism. Also, they are ideally located between the Shakdara and Yezgulem domes to date and identify the nature of the deformation between these domes. We collected paleomagnetic samples from 44 sites through the ~5 km thick volcanoclastic sequence (Fig. S1) to explore any potentially preserved trace of primary magnetization and to assess magnetization directions acquired during the late Cenozoic metamorphic events that were also dated in the present study. We combined rock magnetic analyses with petrologic analyses and multiple radiometric dating techniques, including whole-rock and biotite Ar/Ar and Rb/Sr thermochronology, to time the metamorphic processes and related remanence acquisition in these rocks.

2. Geological setting

2.1. Tectonic setting of the Pamir plateau

The Pamir forms a high plateau extending from the Alai Valley in Kyrgyzstan in the north to the Wakhan Corridor in Afghanistan in the south. It is located at the western extension of the Tibetan-Himalayan orogen (Fig. 1a) and forms a tectonic salient bounded by thrust and transpressional fault systems that juxtapose it with the Tien-Shan to the north and the Tarim and Afghan-Tajik basins to the east and west, respectively (Fig. 1b). The boundary between Pamir and the Southern Tien-Shan to the north is represented by the Main Pamir Thrust, which links with the Darvaz and Kashgar-Yecheng transpressional (KYTS) fault systems in the west and east respectively (Burtman and Molnar, 1993).

Tectonically, the Pamir has generally been subdivided by Paleozoic-Mesozoic sutures into three tectonic regions: the Northern Pamir, Central Pamir and Southern Pamir, the latter of which has sometimes been divided into the Southeastern, Southwestern and Rushan-Pshart zones (Angiolini et al., 2013; Burtman and Molnar, 1993; Robinson, 2015). The Rushan - Pshart zone is often considered as a separate tectonic zone lying between the Central and Southern Pamir (e.g. Schvolman, 1980).

The Northern Pamir, comprising two accretionary *mélange* terranes: the Kunlun terrane in the north and the Karakul-Mazar accretionary wedge in the south, represents the late Paleozoic to early Mesozoic southern active margin of Asia. Although the northwest region of the Northern Pamir was referred to as the Kunlun terrane in earlier works, recent investigations revealed that this terrane has a different geological history from the western Kunlun and should instead be referred to as the Darvaz-Oytag terrane (Li et al., 2020a; Rembe et al., 2021). The boundary between the Kunlun terrane and the Karakul-Mazar complex is represented by the Kunlun suture (Schwab et al., 2004).

The Central Pamir, where the Bartang volcanic rocks crop out, is separated from the Northern Pamir by Tanymas thrust, which overprints the Paleotethys suture zone. The Paleotethys suture zone juxtaposes the Asian rocks in the Northern Pamir with the rocks of Gondwanan affinity in the Central Pamir. The Central Pamir comprises Permian to Cretaceous marine sedimentary rocks and gneiss domes bounded by normal shear zones. The Permian to Cretaceous marine sequence is unconformably overlain by late Cretaceous to early Paleogene volcanic and volcanoclastic rocks. This sequence is finally intruded by late Cretaceous to Neogene plutons and capped by Cenozoic continental sedimentary rocks. The Yazgulom, Sarez and Muzkol gneiss domes of Central Pamir in turn comprise Ediacaran to Triassic strata exhumed from depths of 30 to 40 km along major shear zones (Budanova and Dobretsov, 1991; Schmidt et al., 2011; Stübner et al., 2013b; Rutte et al., 2017b), and from depths of ~75-80 km in the case of the Shatput-Muztaghata dome (Li et al., 2020b). In the south, the Central Pamir is divided from the Southern Pamir by the south-directed Rushan-Pshart thrust, an overprint of the eponymous suture zone.

The Southern Pamir comprises two distinct regions (SW Pamir and SE Pamir), which are separated by a Cenozoic extensional detachment system that developed along the flanks of large crustal domes (Schmidt et al., 2011; Stübner et al., 2013b). The Southeastern Pamir represents a thick Permian to Cretaceous sedimentary succession capped by Cenozoic deposits and deformed into a polyphase fold and thrust belt (Burtman and Molnar, 1993; Vlasov et al., 1991). The Southwestern Pamir comprises Precambrian metamorphic rocks with a Miocene high-grade metamorphic peak and exhumed within the giant Shakh dara dome (Stübner et al., 2013a). The

sedimentary strata and metamorphic rocks of the Southern Pamir are intruded by a belt of Cretaceous arc-related plutons (Aminov et al., 2017; Chapman et al., 2018; Schwab et al., 2004).

2.2. Geology of the Bartang volcanic rocks

Bartang volcanic rocks crop out in the western part of the Central Pamir, on the right bank of the Panj River, along one of its right tributaries - the Bartang River, forming a 200 km long northeast – southwest trending volcanic belt (Fig. 1b,c). This area's geological structure is characterized by Triassic to Upper Cretaceous continental and marine deposits that are overlain by late Cretaceous to early Paleogene volcanic and terrigenous rocks. Plutonic suites of Cretaceous monzonite to granite and Paleogene gabbro to leucogranite intruded the sedimentary and volcanogenic sequences.

The volcanic and volcanoclastic rocks are folded into two synclines that are separated by an anticline composed of upper Triassic dark slate, sandstone and conglomerate. A top-to-the-west thrust fault juxtaposes upper Triassic terrigenous rocks with the Bartang lavas in the east and the Bartang lavas themselves are thrust over Jurassic limestone in the west (Fig. 1c,d). A conformable contact between the limestones and the Bartang lavas is documented west of the eastern syncline (Tajidinov, 1968). However, the age of the limestones underlying the Bartang volcanic rocks is controversial, some argue for an upper Jurassic age and some for an upper Cretaceous age, based on findings of rudist fauna. This controversy led to debates about the age of the Bartang volcanic rocks, which was thought to be either early Cretaceous (Tajidinov, 1968) or early Paleogene (Dronov et al., 1994). The Bartang sequence of volcanic and volcanoclastic rocks is overlain by a Paleogene formation of marl, red conglomerate and sandstone.

The Bartang stratigraphy consists of three units with distinct lithologies (Fig. S1). The lower unit consists of gray to greenish-gray basaltic to andesitic lavas that conformably overlie a thin basal layer of conglomerates. The conglomerates consist of clasts of the underlying limestone (Fig. 2a). The lavas, which form massive layers (500 – 1500 m) are intruded by a couple of small-scale monzonite plutons and overlain by a layer of intermediate and acid tuff. The middle unit starts with a thin basal layer of conglomerates that contains clasts of underlying tuff. Up in the section, the conglomerate is overlain by a layer of tuff intercalated with tuffaceous claystone and siltstone. The next younger layer in the middle unit comprises intercalating polymictic and volcanimictic sandstone and conglomerate. This layer is overlain by tuffs, tuffaceous claystones and siltstones like that underlying it. The upper unit of the Bartang sequence lies on an erosional surface marking a stratigraphic unconformity and starts with a thick layer comprising tuff and

tuffaceous conglomerate of intermediate and acidic composition (Fig. 2b). Upper in the section this unit comprises a relatively thin tuff layer that is overlain by a thick layer of tuff, tuffaceous claystone and siltstone with rare layers of sandstone.

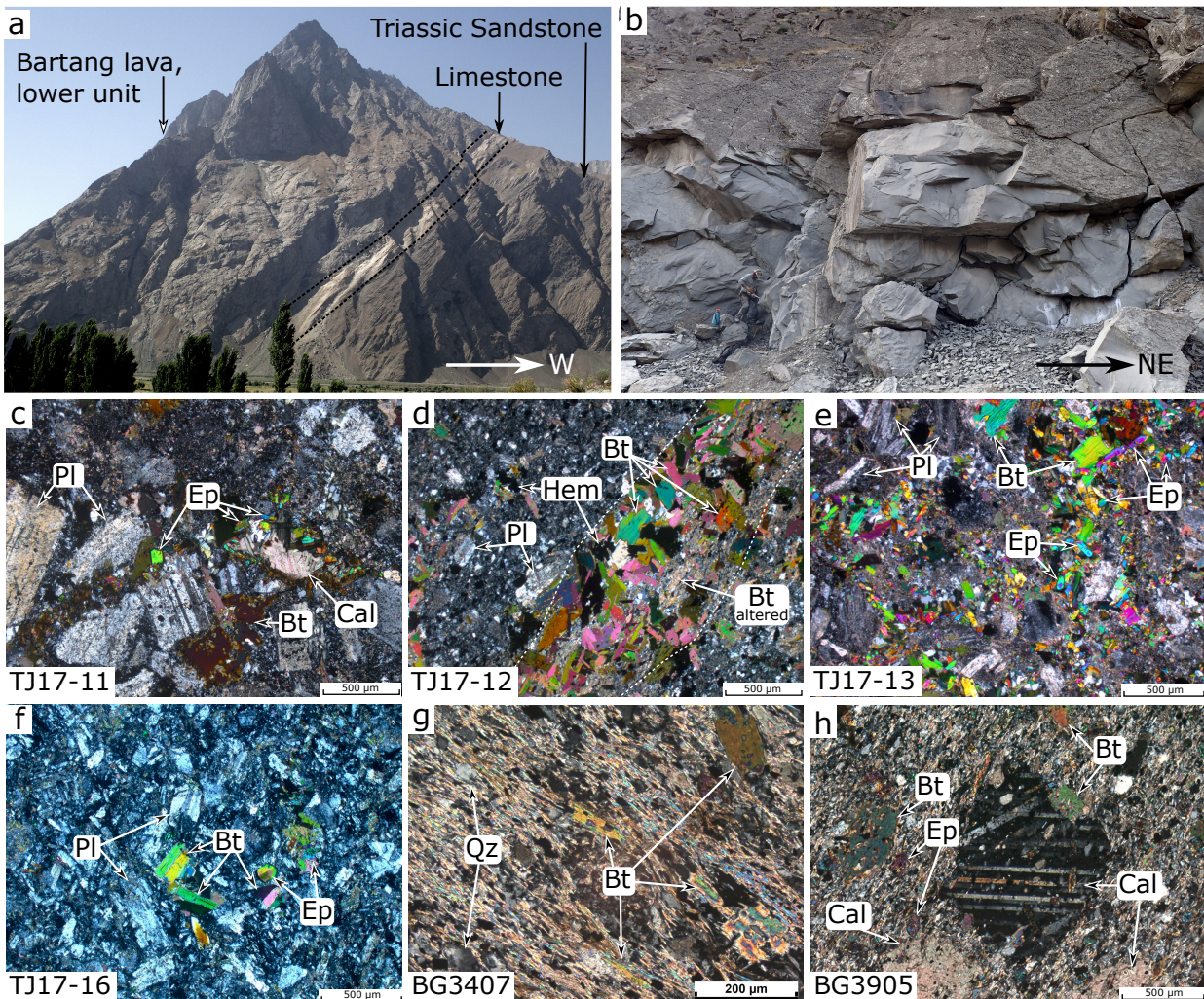


Fig. 2 a) A geological outcrop exposing lavas of the Bartang sequence conformably overlying a limestone of a debated age. b) An outcrop of tuff and tuffaceous conglomerates. c-k) Photomicrographs of petrographic thin-sections. See text and Table 1 for the description of each section. Bt - biotite, Cal - calcite, Ep - epidote, Hem - hematite, Mag - magnetite, Pl - plagioclase, Qz - quartz, Ttn-Hem - titanohematite.

As shown in section 4.1, all rocks are metamorphosed to greenschist facies and contain abundant low-grade metamorphic minerals such as biotite, feldspar, epidote, chlorite, apatite and sometimes calcite. In lavas, grains of metamorphic minerals, especially biotite and epidote, are pervasive and show no or a weakly developed characteristic orientation, whereas in tuffaceous rocks of the middle and upper layers these minerals have a preferred crystallographic orientation

(e.g. Fig. 2g), indicating a deformation event during or after the growth of the metamorphic minerals.

3. Petrography

For this study we examined 16 petrographic thin sections from all three units of the Bartang sequence. Textures and mineralogical assemblages are summarized in Table 1.

Table 1. Texture, phenocryst and groundmass mineralogy, biotite and whole-rock Ar/Ar biotite and Rb-Sr biotite-whole rock ages of the Bartang volcanic and volcanoclastic rocks from the Central Pamir. Mineral name abbreviations after Whitney and Evans (2010).

Sample	Lithology	Texture	Phenocrysts + metamorphic minerals	Groundmass	Ar/Ar age (Ma)	Rb/Sr age (Ma)
Lower unit						
TJ17-10	Basaltic to trachy-andesitic lava	Microlithic porphyritic	Pl+Bt+Mag+Ttn-Hem	Pl+Ep+Bt+Chl+Mag+Ttn-Hem+Qz+Ap	16.46 ± 0.13	
TJ17-11	Basaltic to trachy-andesitic lava	Microlithic porphyritic	Pl+Bt+Mag+Ttn-Hem+Chl+Cal+Ep	Pl+Mag+Ttn-Hem+Ep+Qz+C	16.94 ± 0.12	16.97 ± 0.18
TJ17-12	Trachy-andesitic lava	Microlithic porphyritic	Pl+Bt+Mag+Ttn-Hem	Pl+Mag+Ttn-Hem+Qz	17.76 ± 0.13	
Middle unit						
TJ17-13	Crystal tuff	Microlithic porphyritic	Fsp+Bt+Qz+Ep+Hem	Pl+Ep+Ser+Chl		
TJ17-14	Crystal-lithic tuff	Microlithic porphyritic	Pl+Bt+Ep+Hem+Ap	Pl+Ser		
TJ17-15	Polymictic sandstone	Microlithic porphyritic	Afs+Qz+Bt+Hem+Pl+Am	Qz+Ser		
TJ17-16	Tuff	Porphyritic	Pl+Afs+Bt+Ep+Chl+Hem	Pl+Bt+Ep+Chl+Ap		
BG4405	Crystal - lithic tuff	Porphyritic	Pl+Afs+Bt+Hem+Ep	Pl+Bt+Ep		
Upper unit						

BG0903	Crystal tuff	Aphanitic	Bt+Pl+Qz	Bt+Qz		
BG1607	Tuffaceous conglomerate		Qz+Pl+Bt+Ep			
BG2004	Crystal - lithic tuff	Porphyritic	Pl+Bt+Ep+Qz+Hem	Pl+Ser		
TJ17-18	Tuffaceous siltstone	Porphyritic	Pl+Bt+Ep+Qz	Pl+Ser+Qz+Ep+Hem		
TJ17-24	Crystal tuff	Porphyritic	Pl+Bt+Qz+Ep+Hem	Pl+Ser		
BG3406	Crystal - lithic tuff	Porphyritic	Pl+Bt+Qz+Ep+Hem	Pl+Ser+Ep+Qz+Hem		
BG3406	Crystal - lithic tuff	Porphyritic	Pl+Bt+Qz+Cal+Ep+Hem	Pl+Bt+Ser+Ep+Qz+Hem		
BG3905	Crystal - lithic tuff	Porphyritic	Ap+Cal+Bt+Qz	Ep+Qz+Pl+Bt	15.2 ± 0.1 (Whole-rock; BG3903)	

3.1. Lower unit

The gray to greenish-gray lavas of the lower unit of the Bartang sequence have microlithic porphyritic textures in thin-section. The phenocryst assemblage (30 - 50%) in these samples is mainly represented by eu- to subhedral feldspar (plagioclase and alkali-feldspar), biotite and anhedral to subhedral grains of Fe-Ti oxides represented by magnetite and titano-hematite (Fig. 2c). Feldspar and biotites form large crystals ranging between 0.1 and 1 mm, and 0.1 and 2 mm respectively. Fe-Ti oxides in contrast possess smaller grain sizes of up to 0.4 mm. Sample TJ17-11 also contains secondary calcite, epidote and chlorite minerals. Calcite and epidote are smaller and have grain sizes of up to 0.4 mm. Feldspars are albitized and altered to a dusty mix of sericite. They also contain small inclusions of biotite and an opaque mineral (Fig. S2a). The opaque mineral also appears in thin-sections in the form of small and dispersed grains. The Sample TJ17-10 contains two parts with different types of biotite (Fig. S2b). One part of the thin section contains large, low-Ti, green - light brown, subhedral biotite with small inclusions of quartz and opaque (magnetite + titano-hematite) minerals. This part of the thin-section is highly chloritized with a preferential orientation of the chlorite grains (Fig. S2c), and biotite grains exhibit corrosion features at the contact with the other area (Fig. S2d). The other part of the thin section contains sieve-textured biotite among large eu- to subhedral feldspar crystals showing abundant

polysynthetic twinning. In some samples, biotite is concentrated in 1-2 mm-thick layers, where it occurs in two forms: oriented altered biotite and unoriented fresh eu- to subhedral green biotite (Fig. 2d). The Sample TJ17-11 also contains late veinlets of chlorite + euhedral epidote crystals \pm anhedral calcite (Fig. 2c). Alteration of the feldspars to fine-grained sericite and formation of dispersed opaque minerals may also be related to the formation of these veinlets. Rare crystals of magnetite can also be observed in some samples of this unit. Anhedral to subhedral grains of magnetite contain exsolution lamellae of titanohematite that in turn contain small inclusions of rutile. Titanohematite also forms separate anhedral crystals with sizes of up to 0.4 mm. Rutile inclusions in titanohematite lamellae are small, reaching sizes of up to 0.01 mm. The phenocrysts are set in a fine-grained groundmass of plagioclase, epidote, biotite, chlorite, magnetite, titanohematite and \pm quartz. A few small quartz grains of apatite were also observed in the groundmass. Quartz grains in the groundmass may be devitrification products.

3.2. Middle unit

The middle unit of the Bartang sequence mainly comprises gray, light-gray and greenish-gray tuff and volcanoclastic rocks from basaltic trachy-andesitic to rhyolitic composition. They have microlithic porphyritic textures. The rocks contain between 40 and 60 % of relatively large crystals sitting in a microlithic matrix. Phenocryst minerals are represented by feldspar, biotite and quartz. Secondary minerals are also present in thin-sections that include biotite, epidote, quartz and hematite. Sizes of feldspar phenocrysts range between 0.1 and 1 mm. Some of feldspar grains are albitized and altered to various degrees to fine-grained sericite, with samples TJ17-13 and TJ17-16 representing the most and the least altered samples respectively. The amounts of biotite and epidote grains in samples increase with increased degree of alteration. Green biotite is abundant in sample TJ17-13 (Fig. 2e) containing euhedral stubby epidote inclusions, but it is scarce in sample TJ17-16 (Fig. 2f). Biotite grain sizes vary between tenths of micrometers and 1 mm and together with epidote form clusters and lenses of un-oriented aggregates. Fine-grained biotite crystals also develop and concentrate in the margins of the plagioclase crystals, concentrating on their edges, and show preferential orientation (Fig. S2e). In some samples, both the altered plagioclase crystals and fine-grained biotite grains are deformed and oriented in one direction (Fig. S2f). Some late veinlets are also observed and are filled by fine-grained white mica, euhedral stubby epidote crystals, anhedral opaque minerals, subhedral, large greenish biotite and accessory amounts of quartz. Epidote crystals are eu- to subhedral and are smaller sizes (up to 300 μ m). They have inclusion-rich cores rich in sub-microscopic inclusions, and inclusion-free rims. Quartz

grains also appear in phenocryst assemblages of some the most felsic samples (TJ17-13, TJ17-15). In TJ-15, quartz crystals are large (up to 1mm) and some preserve crystal faces, the latter may be fragments of bipyramidal phenocrysts of high-temperature β -quartz derived from a rhyolite. Hematite is present as anhedral grains of dust size to large sieve-textured clusters to inclusion-free anhedral grains. Inclusions in hematite are dark and anhedral and some of them have an elongate shape. Furthermore, observed in thin-section are also volcanic and sedimentary lithic fragments among the phenocrysts. Volcanic lithic fragments consist of devitrified glass and feldspar grains. Some of the volcanic fragments are fractured and the fractures are filled with fine-grained biotite crystals, which are oriented perpendicular to the strike of the fractures. Some clusters of biotite and epidote have a rounded or ovoid shape. The fine-grained to cryptocrystalline groundmass consists of feldspar, biotite, quartz, epidote, sericite, chlorite and hematite.

3.3. Upper unit

Gray to light-gray crystal and crystal - lithic tuff as well as tuffaceous siltstone of the upper unit of the Bartang sequence have aphanitic and microlithic porphyritic textures with phenocrysts of plagioclase, biotite, quartz, and secondary epidote, calcite and hematite. Besides phenocrysts and secondary minerals, the samples also contain volcanic and sedimentary lithic fragments. The volcanic fragments have mineralogies like those of the host rock, and sedimentary fragments are composed of limestone and arenites with corroded margins. Phenocrysts, secondary minerals and lithic fragments comprise 30 - 60 % of the rocks. Phenocrysts are elongated and define a strong lineation (Fig. 2g and Fig. S2g) indicating syn- to post-emplacement deformation. Eu- to subhedral plagioclase feldspar phenocrysts represent albitized, originally magmatic plagioclase and alkali feldspar. Medium-sized (up to 500 μm) plagioclase crystals in these samples, like those from the middle unit, are altered to fine-grained sericite. Biotites form small (up to 300 μm long) eu- to subhedral greenish-brown and brown crystals that are present in both the volcanic lithic fragments and the host rock. Grain margins of biotites in the host rock and lithic fragments are corroded. Epidote grains are elongate and small (similar to biotite) and locally form clusters, and together with euhedral non-corroded biotite and calcite fill veinlets. In some samples (e.g. TJ17-24) epidote grains occur pervasively throughout the thin-sections and show a weak preferential orientation (Fig. S2h). Calcite forms small (<300 μm) anhedral, roundish grains with corroded margins (Fig. 2h) or euhedral grains that form clusters and fill veinlets. Calcite in the clasts of limestone fragments is eu- to subhedral and small. Quartz grains are small and anhedral. Hematite forms small (<100 μm) anhedral grains and occur clustered and dispersed in the host rock and volcanic

clasts but was not found in sedimentary clasts. The phenocrysts, secondary minerals and lithic fragments are set in a fine-grained to cryptocrystalline groundmass of plagioclase, sericite, epidote, hematite and quartz. Like the phenocrysts, fine-grained biotites define a well-developed lineation in sample BG3407 (Fig. 2g).

4. Geochronology and metamorphic age

Metamorphic ages for four samples from the Bartang volcanoclastic rocks were obtained. For three samples (TJ17-10, TJ17-11 and TJ17-12) we obtained biotite $^{40}\text{Ar}/^{39}\text{Ar}$ ages and for one of them (BG3903) a whole-rock $^{40}\text{Ar}/^{39}\text{Ar}$ age. For the sample TJ17-11 we also obtained a Rb/Sr isochron age calculated from whole-rock and biotite data.

4.1. $^{40}\text{Ar}/^{39}\text{Ar}$ and Rb/Sr thermochronology : Analytical methods

Results presented in section 5 demonstrate that the paleomagnetic samples are remagnetized during a metamorphic event documented petrographically. In order to constrain the timing of this metamorphic event and hence the timing of remagnetization of the Bartang volcanoclastic rocks, we performed $^{40}\text{Ar}/^{39}\text{Ar}$ incremental step-heating on biotite and $^{87}\text{Rb}/^{86}\text{Sr}$ isochron dating on two biotite grain size fractions and a whole rock sample.

Prior to dating, biotite grains were concentrated following conventional magnetic separation procedures and individual grains ranging in size between 125 and 250 microns, as well as whole-rock fragments, were carefully handpicked under a binocular microscope. Pieces of rocks were powdered for $^{87}\text{Rb}/^{86}\text{Sr}$ whole rock isotope analysis.

The $^{40}\text{Ar}/^{39}\text{Ar}$ analyses of biotite grains from three samples (TJ17-10, TJ17-11, TJ17-12) have been performed using the $^{40}\text{Ar}/^{39}\text{Ar}$ dating system at the University of Potsdam. The dating system and the common procedure for $^{40}\text{Ar}/^{39}\text{Ar}$ dating has been described in Wilke et al. (2010) and Halama et al. (2014), and is further described in Supplementary Information.

The $^{40}\text{Ar}/^{39}\text{Ar}$ analyses of a whole-rock millimetric fragment was done using the $^{40}\text{Ar}/^{39}\text{Ar}$ dating system at Géosciences Rennes, following the procedures described in Ruffet et al. (1991, 1995) (Supplementary Information).

Rb-Sr isotope analyses on one whole rock and two biotite specimens from one sample (TJ17-11) were performed at GFZ Potsdam using a Thermo Scientific TRITON thermal ionization mass spectrometer.

Additional information on analytical methods is given in supplementary information.

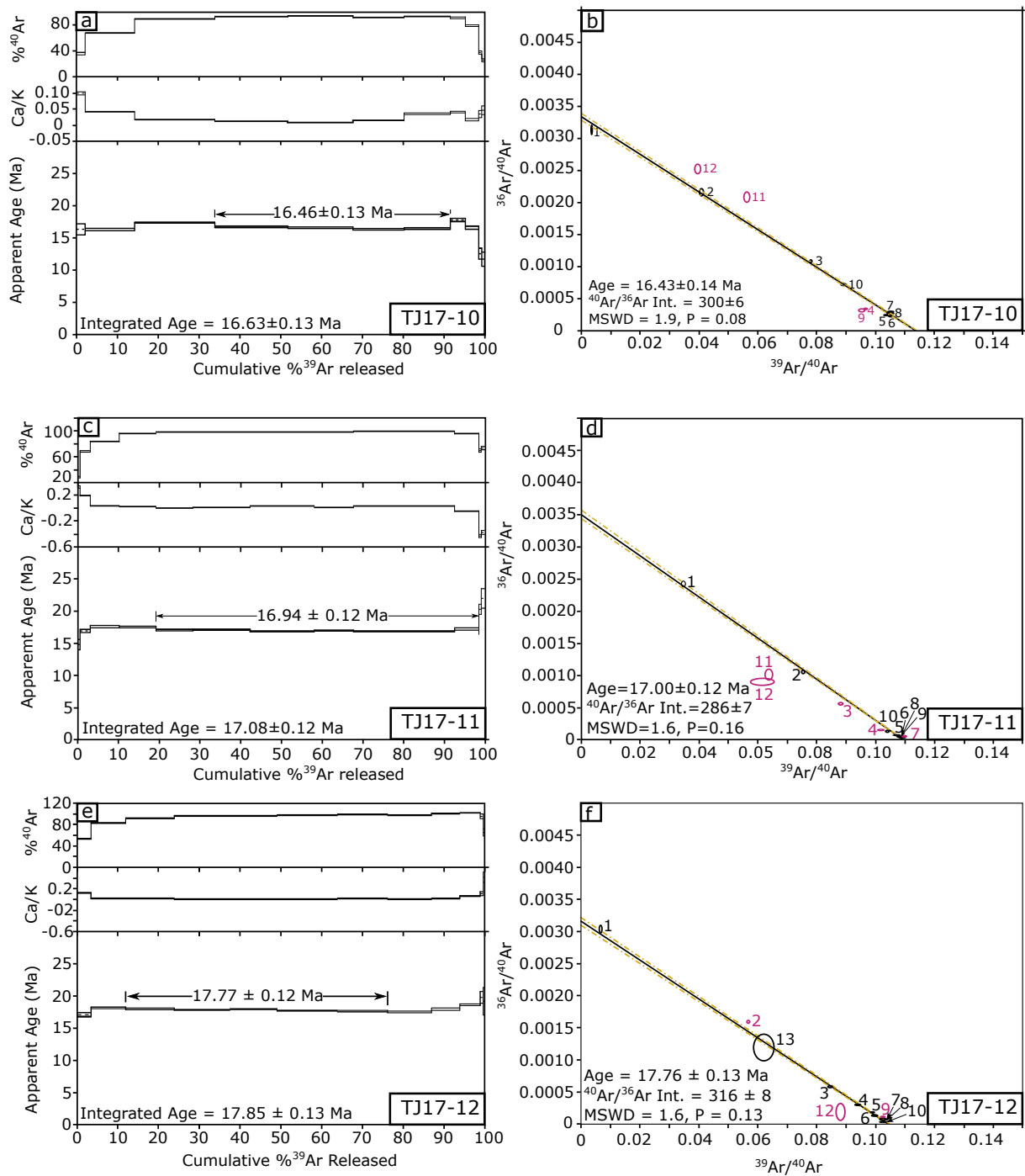


Fig. 3 a,c,e) ⁴⁰Ar/³⁹Ar plateau ages and step-heating spectra for biotite separates from 3 samples (TJ17-10, TJ17-11, TJ17-12 respectively) of Bartang volcanoclastic sequence. b,d,f) Inverse isotope correlation diagrams for the same samples.

4.2 Biotite and whole-rock $^{40}\text{Ar}/^{39}\text{Ar}$ ages

We analyzed biotite mineral separates of about 0.2 mg for each sample by stepwise heating with a CO_2 continuous laser. We obtained a well-defined plateau age of 16.46 ± 0.13 Ma (1 sigma error) for sample TJ17-10 for gas fractions 5 to 8 comprising 57.7 % of the total amount of $^{39}\text{Ar}_K$ released (Fig. 3a and Table S1). The inverse isotope correlation age for all gas fractions, including the plateau defining steps, but excluding data cut off by 5% probability is 16.43 ± 0.14 Ma with an initial $^{40}\text{Ar}/^{36}\text{Ar}$ ratio of 300 ± 6 (Fig. 3b) Uncertainty on the initial ratio (as calculated for the plateau defining steps) is large due to the very small amount of ^{36}Ar , which, however, agrees within analytical uncertainty with the atmospheric value (298.56). Thus, the initial Ar isotope composition is suggested to be atmospheric. Since the plateau and the isotope correlation (inverse isochron) ages agree very well with each other within analytical uncertainty, we prefer the $16.46 (\pm 0.13)$ Ma plateau age for TJ17-10 because of the smaller error.

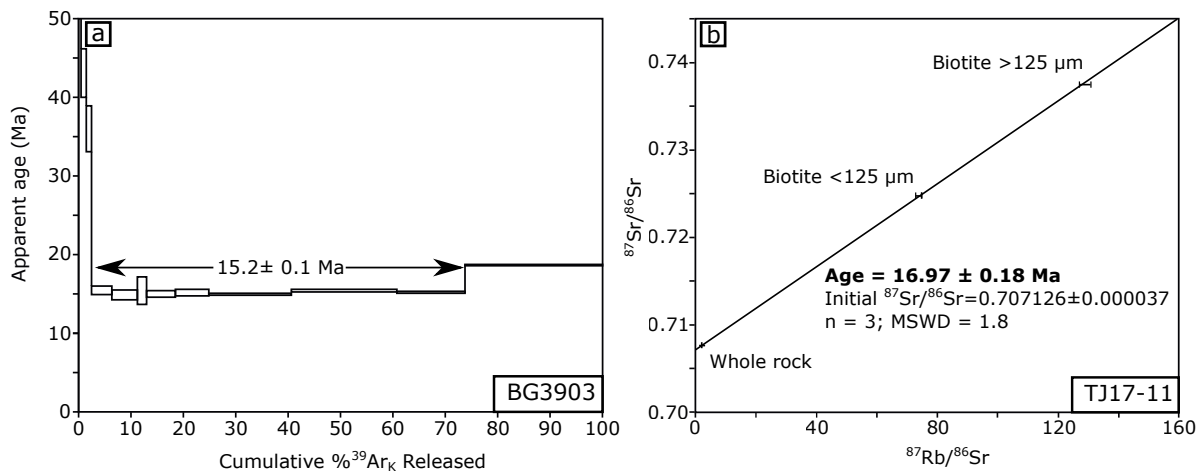


Fig. 4 a) $^{40}\text{Ar}/^{39}\text{Ar}$ plateau age for a whole-rock single fragment from sample BG3903. b) Rb/Sr isochron age from one whole-rock and two biotite grain size fractions for sample TJ17-11.

A well-defined plateau age of 16.94 ± 0.12 Ma (1 sigma error) was also obtained for sample TJ17-11 for gas fractions 5 to 10 comprising 79.3 % of the total amount of released $^{39}\text{Ar}_K$ (Fig. 3c and Table S2). The inverse isotope correlation diagram for all gas fractions, including the plateau defining steps, but excluding the data cut off by 5% probability, yields an age of 17.00 ± 0.12 Ma with an initial $^{40}\text{Ar}/^{36}\text{Ar}$ ratio of 286 ± 7 (Fig. 3d), which agrees with the atmospheric value (298.56) within 2 sigma error. The plateau and the inverse isotope correlation ages obtained for this sample agree very well with each other within error, which allows us to interpret the age of TJ17-11 as the $16.94 (\pm 0.12)$ Ma plateau age.

For sample TJ17-12 we also obtained a well-defined plateau age of 17.77 ± 0.12 Ma (1 sigma error) for gas fractions 4 to 8 that comprise 64.2 % of the total amount of $^{39}\text{Ar}_K$ (Fig. 3e and Table S3). The inverse isotope correlation diagram for all the steps, including the plateau defining steps, but excluding the data cut off by 5 % probability, shows an age of 17.76 ± 0.13 Ma with an initial $^{40}\text{Ar}/^{36}\text{Ar}$ ratio of 316 ± 8 (Fig. 3f). The initial ratio for sample TJ17-12 does not overlap with the atmospheric value (298.56) within 2 sigma error and the initial Ar isotope composition of the sample differed slightly from the atmospheric value. Although the 17.77 Ma plateau age was calculated assuming an atmospheric initial $^{40}\text{Ar}/^{36}\text{Ar}$ ratio, it is indistinguishable from the isotope correlation age. Therefore, for the sample TJ17-12 we prefer the $17.76 (\pm 0.13)$ Ma inverse isotope correlation age.

A well-defined $^{40}\text{Ar}/^{39}\text{Ar}_K$ whole-rock plateau age of 15.2 ± 0.1 Ma (Fig. 4a) (71.5 % of the total amount of $^{39}\text{Ar}_K$ released) was also obtained for sample BG3903. The whole-rock age of 15.2 Ma is noticeably younger than the ages obtained for the biotite grains.

4.3 Whole-rock and biotite Rb/Sr age

We obtained a three-point 16.97 ± 0.18 Ma Rb/Sr isochron age for sample TJ17-11 (Fig 4b) that is consistent with the biotite 16.94 ± 0.12 Ma $^{40}\text{Ar}/^{39}\text{Ar}$ plateau age obtained for the sample (Fig. 3c). The Rb/Sr isochron age was obtained from three measurements - one whole-rock and two biotite grain size fractions. The biotite grains were fresh and represented two size fractions $<125 \mu\text{m}$ and $>125 \mu\text{m}$. A mean square weighted deviation of 1.8 for this isochron indicates a good fit. The initial $^{87}\text{Sr}/^{86}\text{Sr}$ ratio of 0.707126 ± 0.000037 was obtained for the isochron.

5. Paleomagnetism

5.1 Paleomagnetic sampling and methodology

We collected 347 samples from 44 sites, with 6 to 9 samples per site (Table S4). The samples were collected from tuffaceous silt- and sandstones of the middle and upper units of the Bartang sequence for which bedding orientations could be measured. We drilled the samples with a portable drill, orienting them with both a magnetic compass and a sun compass, with the sun compass usage being limited only to the sites with clear visibility of the sun. Where the sun compass readings were not possible, the magnetic orientation was corrected automatically using the declination calculated from the International Geomagnetic Reference Field. The lower unit

lavas are massive thick layers with unclear bedding, which makes them unsuitable for paleomagnetic measurements. However, a few magnetic hysteresis cycles and magnetic susceptibility were obtained for these rocks for comparison with the magnetic properties of samples from the upper unit. In addition, a few samples of this unit were collected for petrographic study.

The remanent magnetizations were measured with a 2G cryogenic magnetometer installed in a shielded room (Université de Rennes, France). More information about the laboratory procedures is given in the Supplementary information.

5.2 Magnetic properties

All samples except those from one site (BG39) have low intensities of natural remanent magnetization (NRM; $\sim 0.008 \text{ Am}^{-1}$) (Fig. 5a, Table S4) and low magnetic susceptibilities ($150\text{--}250 \cdot 10^{-6} \text{ SI}$).

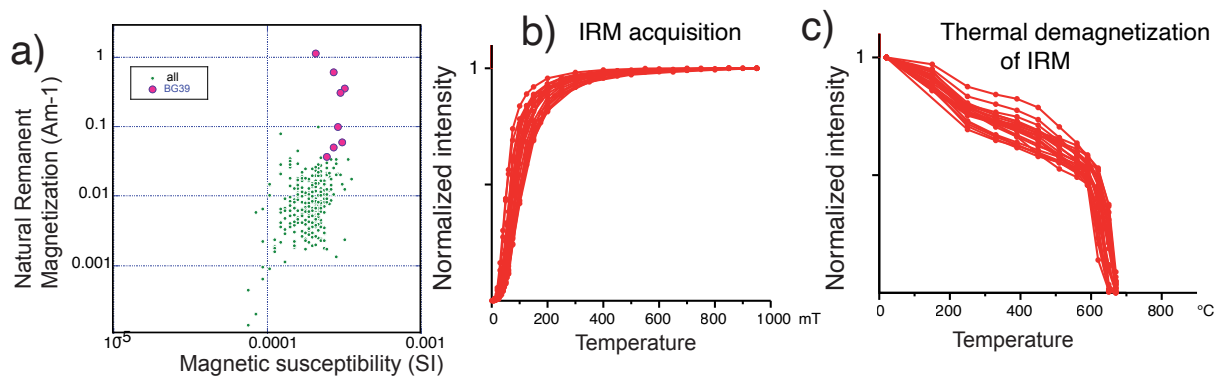


Fig. 5 a) Plot of the intensity of the NRM versus magnetic susceptibility. b) Plot of IRM acquisition and c) thermal demagnetization of the IRM.

Acquisition of isothermal remanent magnetization (IRM) indicates near saturation above 600 mT (Fig. 5b, supplementary Fig. S3). Less than 10% of the IRM is acquired below 30 mT suggesting magnetite is not a dominant magnetic carrier. AF demagnetization of IRMs acquired in 1 Tesla provides a similar range of remanent coercivities with 50 to 90% of the IRM removed by 150 mT AF demagnetization (supplementary Fig. S4a). Hysteresis data from 24 samples confirm the high coercivity field above 50 mT and up to 170 mT (supplementary Fig. S5). These samples have low B_{CR}/B_C values (median 1.15) and high ratio of M_{RS}/M_S of 0.75. MPMS measurements of high field (2.5 T) IRMs acquired at low temperature (10 K) show no evidence for the classic transitions due to hematite (Morin transition) or magnetite (Verwey transition)

(supplementary Fig. S4b). The Zero Field Cooled and Field Cooled (ZFC/FC) curves are similar and we can thus discard the presence of goethite in these samples.

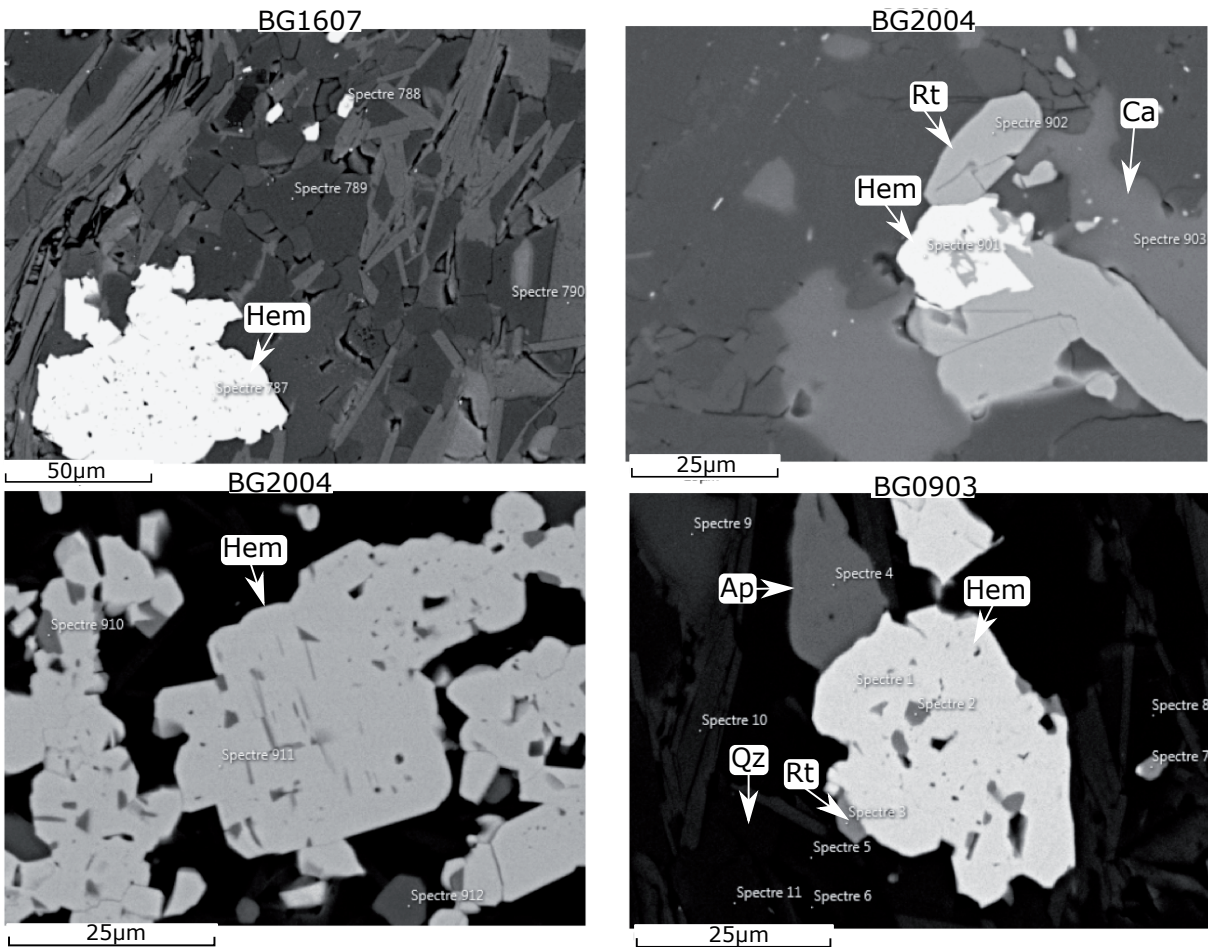


Fig. 6. Examples of SEM images. All samples contain quartz, calcite, biotite and oxides. Large grains (~25 µm) of titanohematite are the dominant oxides. Rutile inclusions are numerous in the hematite grains. EDS data are given in supplementary information.

Thermal demagnetization of IRMs acquired at 1T shows a main unblocking temperature between 610-650°C (Fig. 5c) while a secondary phase is demagnetized between 150 and 250°C. Unblocking temperatures of IRM and of the NRM are lower than the Néel temperature of hematite. This indicates that the magnetic carrier is not pure hematite. K(T) experiments confirm the presence of two magnetic phases with the main phase having a Curie temperature similar to the unblocking temperature of the IRM (supplementary Fig. S6). These properties are found in the tuff and volcanoclastic sediments. Magnetite is however the main magnetic phase in the massive lavas of the lower unit (supplementary Fig. S6). Acquisition of thermoremanent magnetization

(TRM) in the laboratory in a 50 μT field gives TRM values of $\sim 0.5 \text{ Am}^{-1}$ in volcaniclastic samples. Site BG39 is the only site with NRM intensity of the same magnitude as a TRM.

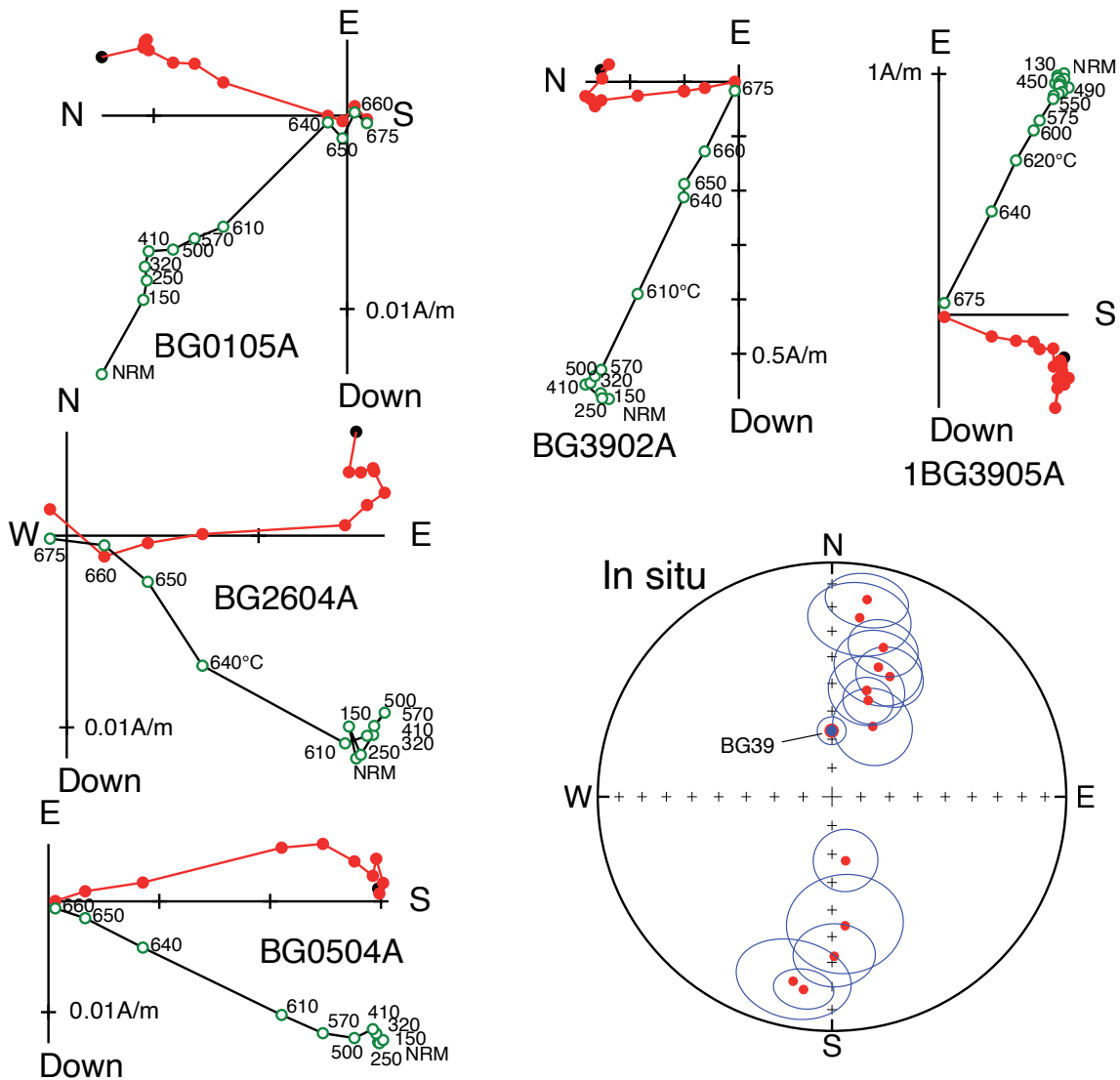


Fig. 7. Examples of orthogonal plots of thermal demagnetization data for 5 samples in in-situ coordinates. Red filled (open green) circles are projections onto the horizontal (vertical) planes. The site mean directions with their 95% confidence circles are displayed on the equal-area stereonet. Filled circles are projections in the lower hemisphere (positive inclination).

5.3 SEM/EDS data

Microscope images in reflected light indicate that secondary titanohematite is the main iron oxide in the samples and its irregular shape indicates recrystallisation. To better describe the

magnetic carriers, five thin sections were studied under a Scanning Electron Microscope, equipped with an EDS detector (Fig. 6 and supplementary Fig. S7 for EDS spectra), to estimate the composition. In all cases, the main oxides are titano-hematites ($\text{Fe}_{2-y}\text{Ti}_y\text{O}_3$) with y ranging from 0.07 to 0.23 and a mean value of 0.13 from 17 analyses. Estimates of y from EDS data are less accurate than with electron microprobe analyses but agree with the observed unblocking temperatures of the magnetization as a “ y ” value of 0.1 leads to a Curie temperature of about 590°C (Hunt et al., 1995).

Large rutile inclusions are found in most of the titano-hematite crystals, but we did not observe ilmenite lamellae in the samples. The resolution of the SEM is not sufficient to discriminate the composition of very thin lamellae ($< 1 \mu\text{m}$ thick) between rutile and ilmenite.

5.4 Characteristic directions

Most samples provided complex thermal demagnetization diagrams and a large scatter at the site level. Only 14 sites rendered apparent ChRMs with unblocking temperatures above 570°C and within site coherency to enable the determination of a mean direction (Fig. 7, Table S5). The mean directions are distributed along a girdle indicating that these directions do not represent the paleofield record (Fig. 7). Site BG39, which has a stronger NRM, provided more stable ChRMs. However, remagnetization is likely because two magnetization components display antiparallel directions within this site and these directions are close to a late Cenozoic paleo-field in in-situ coordinate. Field evidence, such as a dike intrusion that could explain a remagnetization event was not observed in the field.

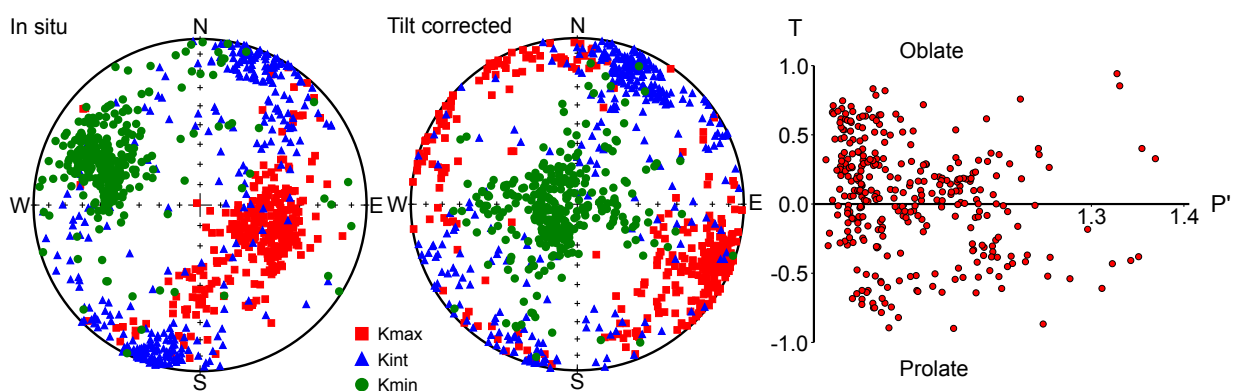


Fig. 8. Directions of the main axes of the AMS ellipsoids from Bartang samples in in-situ and tilt corrected projections (all symbols plotted with positive inclinations). Right) T - P' plot showing the shape of the ellipsoids defined by the parameter T (Jelinek, 1981) versus the corrected anisotropy degree P' .

5.5 Magnetic fabric

The anisotropy of magnetic susceptibility (AMS) was measured on 278 samples. The magnetic foliation dips to the E-SE with a steeply plunging magnetic lineation in in-situ coordinates (Fig. 8, supplementary Fig. S8, Table S6). The shapes of the magnetic ellipsoids vary from oblate to prolate. The Bartang sequence is folded into a tight syncline with overturned beds on the eastern side but the AMS is well organized in in-situ coordinates, in agreement with a magnetic fabric controlled by the tectonic and metamorphism related schistosity observed in the orientation of the fine-grained biotites.

In addition to iron oxides, paramagnetic minerals such as biotite contribute significantly to the AMS fabric due to their magnetic anisotropy (Borradaile and Werner, 1994, Martin-Hernandez and Hirt, 2003) and their importance in volume. In order to assess the magnetic anisotropy due to oxides, we have carried anisotropy of IRM in a field of 950 mT and anisotropy of TRM acquired in a low field (50 μ T) by cooling below 670°C (supplementary Fig. S9). The degree of IRM anisotropy is stronger and up to 2.0. While the magnetic foliation is also dipping to the E-SE similar to the AMS foliation, lineations of anisotropy of TRM and IRM are distributed along a girdle. Measurements of the AMS on samples previously thermally demagnetized provide also a tighter AMS magnetic foliation than the one measured before the thermal treatment (supplementary Fig. S10) suggesting that the natural remanent magnetizations contribute slightly to the scatter seen in the AMS data.

5.6 Field-impressed AMS

To check the control of remanent magnetizations on the AMS, we also made AMS measurements in samples with IRM. The IRM was changing the AMS fabric with a minimum axis toward the direction of the IRM (Fig. 11a, c). The AMS fabric was measured after each step of IRM acquisition. The magnitude of the induced magnetic fabric increases with the imparted field and mirrors the IRM acquisition curve (Supplementary Fig. S11). Subsequent applications of an IRM along either X, Y, Z will rotate the minimum axis of the IRM according to the IRM direction (Supplementary Fig. S12).

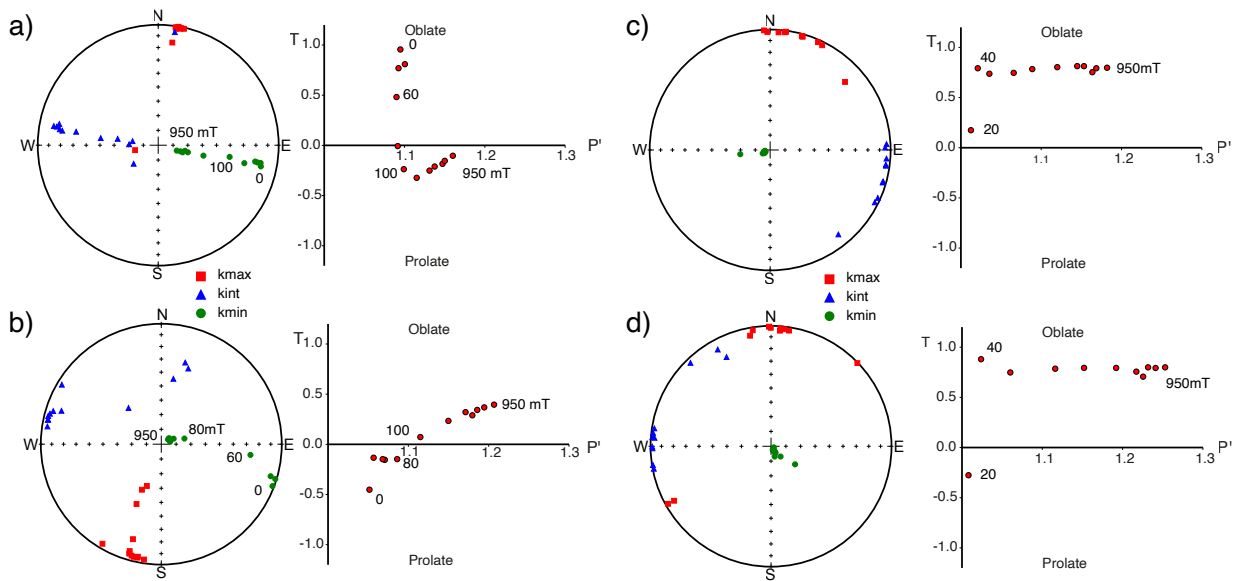


Fig. 9. Plot of the ellipsoids of the AMS (equal area plot of the principal directions and T - P' plot) measured at each step of IRM acquisition up to 950 mT along the z axis in sample coordinate for specimen BG3407a (a) (previously thermally demagnetized at 670°C) and a second specimen not demagnetized BG3407b from the same core (c); b, d) difference tensor after subtracting the initial AMS prior to IRM acquisition for each specimen as in (a) and (b). Data shown in sample coordinates

This effect has been described for single domain magnetite (Potter & Stephenson, 1990a) and hematite (Fuller, 1963) but the magnitude of the field-impressed AMS was relatively low. In the present study, the impact of an IRM upon the AMS fabric is huge. Paramagnetic silicates and iron oxides both contribute to the AMS fabric. In order to remove the contribution of the paramagnetic signal and better highlight the effect of the IRM, the initial AMS was subtracted from the tensor after IRM acquisition. This procedure does not inform on the magnetic susceptibility fraction carried by the oxides versus the paramagnetic minerals as it also removes the initial AMS carried by the iron oxides. Despite the difficulty to estimate the contribution of oxide minerals to the initial AMS, the field-impressed AMS calculated by difference tensors (Fig. 11) is a mainly oblate fabric with the minimum axis in the direction of the applied field. Indeed, the AMS minimum axis rotates progressively toward the direction of IRM with increasing field values (Fig. 9a, c). The increasing magnitude of the field-impressed fabric is however better observed after subtraction of the initial AMS fabric. The shape of field-impressed AMS from the difference tensor does not change significantly (Fig. 11 b,d).

The lava flows and tuff layers of the lower and middle unit of the Bartang sequence were not sampled for paleomagnetic but for petrological studies. Magnetic susceptibilities were measured on fine rock powders from 6 samples. Samples from the flows TJ17-10 and TJ17-11 have high magnetic susceptibilities with magnetite as the main carrier. Samples from the tuffs TJ17-13, TJ17-14 and TJ17-16, however, present magnetic susceptibilities within the range observed in samples from the upper Bartang unit. AMS and IRM measurements were made on compacted powder. Sample TJ17-16 presents the highest IRM induced AMS fabric with an anisotropy degree of 1.8. Such effect was almost suppressed by an AF demagnetization at 150 mT.

Five samples in red sandstones from the Tadjik basin with detrital hematite as the main magnetic carrier were also processed for comparison (Supplementary Fig. 11). IRM acquisition do not saturate in a field > 2 Teslas. The degree of field-impressed AMS is much lower and no greater than 1.03.

6. Discussion

6.1. Metamorphic facies and its timing

The Bartang sequence mainly comprises gray, light-gray and greenish-gray tuff and volcanoclastic rocks that have microlithic porphyritic textures. The rocks contain between 30 and 60% phenocryst and metamorphic minerals, which include plagioclase, biotite, epidote, quartz and hematite ± calcite ± apatite ± sericite ± amphibole. This mineral paragenesis is typical of greenschist facies, which forms at around 250-400 °C and 3-4 kilobars (Spear, 1994). Green biotite and epidote clusters with rounded and void shapes are thought to be metamorphosed amygdules filled with secondary minerals quickly after the volcanic rock cooled and that later altered to a greenschist facies assemblage by high temperature hydrothermalism (e.g. Fodor et al. 1981). These observations are consistent with suggestions by Puzankov et al. (2000) that the Bartang volcanic rocks erupted in an aqueous marine setting, with only some upper layers being deposited subaerially. On the other hand, metamorphic biotite and epidote concentrations inside mm-thick veinlets imply that metamorphic minerals filled open fractures. Metamorphic fluids could also lead to the formation of round clusters of green biotite and epidote within the pores of volcanic rocks. Moreover, the orientation of fine-grained, parallel metamorphic biotite crystals that developed in and partly replaced outer rims of feldspar (plagioclase) (Fig. S2e) is indicative of a deformation event synchronous with the formation of this secondary biotite. Geologic

observations show that this event is related to NW-SE folding and thrusting (Fig. 1d). Similarly, oriented and elongated secondary metamorphic biotite grains, observed in the rocks of the upper unit (Fig. 2g and Fig. S2f-g), demonstrate a well-defined deformation event contemporaneous with the biotite formation at 15.2 Ma based on the whole-rock $^{40}\text{Ar}/^{39}\text{Ar}$ age (Fig. 3). To conclude, while the emplacement age of the volcanic rocks is thought to be late Cretaceous - early Paleogene (Dronov et al., 1994; Puzankov et al., 2000; our data in preparation), dating the first stage of hydrothermalism to this time, our biotite and whole-rock $^{40}\text{Ar}/^{39}\text{Ar}$ and Rb/Sr ages place the second stage in the middle Miocene (15 - 18 Ma) related to the NW-SE shortening event.

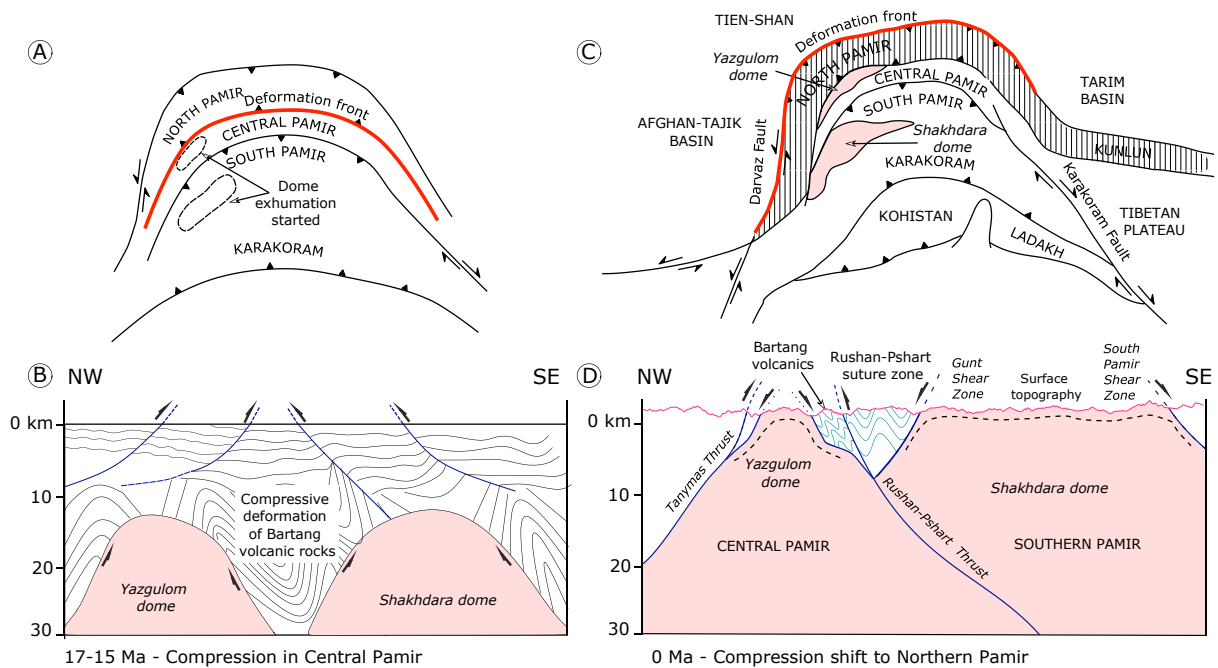


Fig. 10. A schematic tectonic model of the Pamir orogen in Miocene, illustrating compressional deformation between the Shakh dara and Yazgulom domes. Location of shear zones and thrust faults is taken from Stübner et al. (2013a) and Vlasov et al. (1991).

The Bartang volcanic sequence is located between two large-scale gneiss domes (Yazgulom to the north and Shakh dara to the south) (Fig. 1) that exhumed deep crustal rocks (from depth of 30 - 40 km) to the Earth surface (e.g. Schmidt et al., 2011; Stübner et al., 2013a; Stearns et al., 2015). These crystalline domes, similar to the Muzkol, Sarez and Muztagh-Ata domes in the eastern Pamir, contain Barrovian facies-series with peak metamorphic assemblages of garnet + kyanite ± staurolite + biotite + oligoclase ± K-white mica. Peak metamorphic conditions in the Miocene at around 20 Ma were 9.4 kbar and 588°C for the Yazgulom dome and 6.5 - 14.6 kbar and 750°C for the Shakh dara dome (Grew et al., 1994; Schmidt et al., 2011; Stübner et al., 2013a). Exhumation of these gneiss domes was preceded by a phase of burial, which lasted from >35 to

22 Ma in the eastern Pamir. $^{40}\text{Ar}/^{39}\text{Ar}$ dating of white micas and biotites for the gneiss domes at Sarez and Muzkol located north of the Rushan-Pshart fault system yield the same age we obtained (~18-15 Ma) for Bartang samples (Rutte et al., 2017a). Lukens et al. (2012) report single grain total fusion $^{40}\text{Ar}/^{39}\text{Ar}$ ages on detrital white micas from 5 samples of sands from the five rivers draining the Central Pamir and the northern Southern Pamir (Gunt river). Results from the detrital micas from the river draining the Muskol dome agree with those of Rutte et al. (2017a). Detrital mica ages from the Gunt River south of the Rushan-Phart suture are also similar to the ages found in the Bartang samples. In contrast, ages of detrital white micas from the river draining the Yazgulom dome are slightly older with peaks at ~19 Ma and ~27 Ma. Results in detrital white micas from the Bartang river have a wide range of argon ages that vary between 14 Ma to 205 Ma, showing that the Central Pamir east of our study area does not record the same intense deformation during the early Miocene.

6.2. Magnetic properties under metamorphic conditions

Secondary Ti-poor titanohematite is the main oxide mineral in the volcanoclastic and tuff samples. The characteristic directions that have been determined, have unblocking temperatures above 600°C which is larger than expected for the greenschist facies metamorphism found in the samples. The remanent magnetization is thus not a simple thermal remanent magnetization but involves more complex chemical magnetization. The formation of titanohematite grains with rutile inclusions likely occurred during metamorphism possibly by transformation of previous igneous magnetite/titano-magnetite in the original volcanoclastic rocks. The intensity of the NRM (0.01 Am^{-1}) is much lower than a laboratory TRM ($\sim 0.4 \text{ Am}^{-1}$) acquired by cooling below 660°C in a field of 50 μT . The mean-site directions at 14 sites, distributed within a foliation plane, cannot be considered as stable chemical ChRMs related to a paleofield during the growth of the titanohematite grains. Site BG39 is a noticeable exception, where both normal and reverse ChRMs were found. Samples from this site have similar magnetic properties as the other samples, but, in contrast to other samples, the NRM and laboratory TRM intensities of these samples are within the same order of magnitude. Two samples have reverse polarity magnetization, 4 have a normal polarity magnetization while 2 samples have intermediate directions in between the normal and reverse polarities. The existence of both polarities within the same site permits to discard the hypothesis of a local heating event due to, for example, dike intrusion. The two samples with intermediate directions show also evidence for both polarities within the sample.

Self-reversal is one of the most striking properties of the titano-hematite but when the bulk composition of the titano-hematite is near $y = 0.5$. Moreover, such a composition is found only in rapidly quenched pyroclastic rocks (Nagata and Uyeda, 1959). This is not the chemical composition of the Bartang samples and self-reversal was not observed during the laboratory TRM acquisition. However, unusual properties were found on ilmeno-hematite lamellae with lower y values (Carmichael, 1961, Merrill and Gromme, 1969). The concept of lamellar magnetism (McEnroe et al., 2009; Robinson et al., 2002) has been recently advanced to explain the strong magnetization observed in titano-hematites with nanometers size lamellae. The rocks carrying these highly oxidized iron oxides such as granulite facies rocks in the Adirondacks (McEnroe and Brown, 2000) or upper amphibolite facies rocks in southern Sweden (McEnroe et al., 2001) and Norway are higher-grade metamorphic rocks than the Bartang rocks. We did not acquire sufficient high-resolution SEM images to detect submicron size ilmenite lamellae and TEM images are likely necessary to test the hypothesis of lamellar magnetism in the samples (McEnroe et al., 2009). The mean direction at site BG39 is close to the expected mid-Miocene direction and we therefore speculate that the Bartang sequence did not record major tilt or rotation since the time of cooling at ~ 16 Ma. This speculation is however based on one site and further work is needed.

The AMS fabric is characterized by a magnetic foliation and a steeply dipping lineation toward the E-SE and this fabric was acquired during deformation. There are significant variations in the shape of the ellipsoids with prolate or oblate fabrics (Fig. 8). But for samples previously thermally demagnetized, the fabric is mainly oblate with a well-defined magnetic foliation (supplementary Fig. S10). It is well known that thermal enhancement of magnetic susceptibility after heating in the laboratory also enhances the degree of anisotropy (Henry et al., 2003; Roperch et al., 2010). In the present study, there is no evidence for significant changes in the magnetic properties of the samples except for samples from site BG39. The changes in the magnetic fabric after heating the samples above 600°C could be related to a slight control of the remanent magnetization on the magnetic susceptibility in samples prior to the heating treatment. We thus made AMS measurements during the acquisition of a laboratory remanent magnetization (IRM). We have found evidence for a very high field-impressed AMS after IRM acquisition. As already pointed out by Rochette et al. (1992), the effect of a remanent magnetization on the AMS has been neglected by paleomagnetists. Only a few studies report AMS changes after direct fields applications especially in magnetite-rich samples (Potter & Stephenson, 1990a). Schmidt & Fuller (1970) reported such anisotropy in large single crystals of hematite. An oblate fabric during IRM acquisition was also reported for one sample of hematite ore (Zapletal & Kropáček, 1985). In the Bartang samples, the size of the Ti-poor titano-hematite grains is usually below $100\ \mu\text{m}$. Further

work is needed on metamorphic rocks, but the initial chemical composition and the P/T degree of metamorphism are likely key parameters to produce titano-hematite grains with such large field-impressed AMS. Lanci (2010) interpreted IRM impressed magnetic foliation in glassy volcanics from pillow lavas as evidence of multi-axial anisotropy in single domain titanomagnetite. Large field-impressed AMS fabric is observed in a wide range of rocks from rapidly cooled volcanic rocks to pyrrhotite-rich metamorphic rocks where single domain grains are the main magnetic carrier, and in general we observe that the intensity of the IRM controls the field-impressed AMS (Roperch et al., submitted). IRM impressed AMS is also observed in several types of red beds with hematite as the main carrier, but the degree of anisotropy of this induced fabric is usually between 1.01 and 1.02 (Supplementary Fig. S12 and Roperch et al., submitted). The effect measured in the Bartang samples with metamorphic titanohematite is 10 to 20 times higher than in samples with hematite and we speculate that the impressed AMS may have some link with lamellar magnetism at the interface of thin ilmenite or rutile lamellae within the hematite in oxidized greenschist facies metamorphic rocks.

6.3. Tectonic implications

The AMS fabric presents a steeply dipping foliation plane that reflects the development of schistosity during greenschist metamorphism as observed in thin sections (sample BG3407, Fig. 2). This incipient schistosity was likely acquired during the phase of NW-SE compressive deformation leading to folding and thrusting of the Bartang sequence. The AMS foliation is dipping E-SE in agreement with the main orientation of the folds and thrusts not only affecting the Bartang units but also the Triassic rocks in between the Bartang valley and the Rushan-Pshart suture zone. Compressive structures within the Gunt shear zone also have a SW-NE orientation (Worthington et al., 2020) (Fig. 1). The shortening phase is likely related to prograde metamorphism of the gneiss domes. $^{40}\text{Ar}/^{39}\text{Ar}$ ages provide an age constraint on this event. The $^{40}\text{Ar}/^{39}\text{Ar}$ ages obtained on biotites from the Bartang volcanoclastic rocks are similar to biotite $^{40}\text{Ar}/^{39}\text{Ar}$, garnet Lu-Hf/Sm-Nd, monazite U-Th-Pb, and titanite U/Pb ages reported for most gneiss domes in the surrounding area (Yazgulom, Sarez, northern part of the Shakh dara dome) (Hacker et al., 2017; Searle and Hacker, 2018), suggesting a pervasive metamorphic event at the regional scale.

Although it has been suggested that the Pamir orogen has experienced a phase of crustal extension from 20 Ma to 12 Ma (Rutte et al., 2017a; Stübner et al., 2013a), the metamorphism affecting the Bartang volcanic rocks in between the Yazgulom and Shakh dara domes suggests a

compressive deformation. This is consistent with the interpretations of Searle and Lamont (2019) suggesting that metamorphic core complexes of the Pamir orogen formed due to exhumation driven by crustal thickening in a generally compressional tectonic setting (Figure 10). The co-occurrence of extension and compression is more difficult to account for in a generally extensional setting such as resulting from regional lateral extrusion or slab delamination (Chapman et al., 2017; Kűfner et al., 2019).

The strike orientations of the main structural trend observed to the west of the Central Pamir and south of the Yazgulom dome are compatible with the magnetic foliation recorded in the Bartang valley. To constrain the timing of this strike orientation results and to test whether it results from a vertical-axis rotation, we can rely only on the one paleomagnetic site (BG39) interpreted as a magnetization recorded after tilting because the direction is in the expected direction before any tilt correction. Taking this site at face value, would suggest no tectonic rotation or tilt affected these rocks after cooling and metamorphism. This would imply no oroclinal bending of the inner Pamir since the 17-15 Ma metamorphic event, assuming the latter tilted the rocks and the magnetization was acquired upon cooling at the end of the metamorphic event. However, we cannot reject the hypothesis of a vertical-axis rotation affecting the rocks before or during the metamorphic event. A primary magnetization acquired before the regional metamorphism could record such a rotation but primary magnetizations have been hard to find in the Pamir affected by secondary overprints due to metamorphism (Waldhör et al., 2001. counterclockwise rotation of the AMS bringing a foliation dipping to the south to its present in situ orientation prior to cooling at 17-15 Ma. At this stage, we can only suggest that the curvature of the structures within the Western Pamir either occurred mainly prior to this time or is an old original inherited shape that has not been bent during the Pamir indentation. Further paleomagnetic study in rocks over the area affected by various degree of metamorphism is needed to confirm the single result observed at site BG39 suggesting that the whole area did not record significant local rotation or tilt following the 17-15 Ma deformation. As the magnetic carrier in the lavas is magnetite and not titanohematite, a less complex chemical magnetization may be recorded in the lavas than in the volcanoclastic sediments.

Taken together our results showing contractional deformation until 15 Ma followed by no vertical-axis rotation and tilt, are consistent with the view that contraction jumped northwards from the Southern and Central to the Northern Pamir during the Middle Miocene (e.g. Rűtte et al. 2017a; Hacker and Searle, 2018), as suggested by provenance analyses in the Tajik foreland basin indicating a drastic increase in sediment accumulation and a shut off of Central and South Pamir zircon sources replaced by North Pamir sources (Li et al., 2021).

7. Conclusions

The Bartang volcanic rocks contain a metamorphic mineral assemblage typical of greenschist facies metamorphism. This assemblage is represented by plagioclase, biotite, epidote, quartz and hematite \pm calcite \pm apatite \pm sericite \pm amphibole reflecting temperatures of 250-400°C and pressures of 3-4 kilobars. Development of secondary metamorphic biotite within veinlets also indicates syntectonic growth of metamorphic minerals, which can be attributed to a metamorphic event that, according to our new biotite and whole-rock $^{40}\text{Ar}/^{39}\text{Ar}$ and Rb/Sr ages, took place at 17-15 Ma. Thus, we conclude that the Bartang volcanic rocks underwent a regional metamorphism during the mid-Miocene in relation to the emplacement of the Yazgulom and Shakh dara gneiss domes (Fig. 10). GPS data (Zhou et al., 2016) indicate that the present-day shortening is now related to the Main Pamir thrust and with probably little deformation between the Central and Southern Pamir (Fig. 10).

Magnetic characteristics and secondary electron microprobe investigations revealed that Ti-poor titanohematite is the main magnetic carrier in the rocks. It contains 10 to 20% ilmenite in solid solution, although only rutile inclusions were detected. The anisotropy of magnetic susceptibility (AMS) exhibits a well-defined foliation plane and steeply plunging magnetic lineation. The anisotropy ellipsoids change from oblate to prolate and the degree of AMS in the rocks approaches 1.4 in some samples. With a magnetic lineation spread in the anisotropy foliation, the anisotropy of high field isothermal remanent magnetizations or thermoremanent magnetizations has a substantially greater anisotropy (up to 2.0). We contend that anisotropy has a considerable influence on the scatter of natural remanent magnetization. But the natural remanent magnetization also affects the AMS as the AMS is mainly oblate in thermally demagnetized samples. Laboratory IRM acquisition demonstrates that these rocks with titanohematite carriers have strong-field remanent magnetizations impressed AMS. Ti-poor titanohematite may be a major underappreciated oxide in volcanoclastic rocks metamorphosed under greenschist facies conditions, and strong field-impressed AMS fabric may be an interesting diagnostic of such metamorphism.

AMS data support a metamorphic event under a tectonic regime of local compressive deformation in the NW-SE direction. The pervasive metamorphic event under greenschist facies conditions in the Bartang valley is contemporaneous with the exhumation of gneiss domes in the Central and Southern Pamir.

8. Acknowledgements

This project was funded by the Agence Nationale de la Recherche (<https://anr.fr/Projet-ANR-13-BS06-0012>) Jovid Aminov received support from Chinese Academy of Sciences's President's International Fellowship Initiative (2019PM0039). GDN acknowledges funding from ERC grant MAGIC 649081. The acquisition of the VSM8600 used at the Laboratoire des Sciences du Climat et de l'Environnement (LSCE) for the hysteresis measurements was financially supported by the Paris Ile-de-France Region – DIM “Matériaux anciens et patrimoniaux”, the Institut National des Sciences de l'Univers (INSU) and the LSCE. We would like to thank Loïc Joanny and Francis Gouttefangeas of ScanMAT/CMEBA for their help with the electron microscope. We are grateful to Professor Samuel Angiboust for his editorial handling of this manuscript. We also appreciate the insightful feedback and suggestions from Professor Jiří Žák and Dr. Yipeng Li on the previous versions of this manuscript.

References

- Aminov, Jovid, Ding, L., Mamadjonov, Y., Dupont-Nivet, G., Aminov, Jamshed, Zhang, L.-Y., Yoqubov, S., Aminov, Javhar, Abdulov, S., 2017. Pamir Plateau formation and crustal thickening before the India-Asia collision inferred from dating and petrology of the 110-92 Ma Southern Pamir volcanic sequence. *Gondwana Res.* 51, 310–326. <https://doi.org/10.1016/j.gr.2017.08.003>
- Angiolini, L., Zanchi, A., Zanchetta, S., Nicora, A., Vezzoli, G., 2013. The Cimmerian geopuzzle: new data from South Pamir. *Terra Nova* 25, 352–360. <https://doi.org/10.1111/ter.12042>
- Bazhenov, M.L., 1996. Permo-Triassic paleomagnetism of the North Pamir: tectonic implications. *Earth Planet. Sci. Lett.* 142, 109–120. [https://doi.org/10.1016/0012-821X\(96\)00090-8](https://doi.org/10.1016/0012-821X(96)00090-8)
- Borradaile, G.J., Werner, T., 1994. Magnetic anisotropy of some phyllosilicates. *Tectonophysics* 235, 223–248. [https://doi.org/10.1016/0040-1951\(94\)90196-1](https://doi.org/10.1016/0040-1951(94)90196-1)
- Budanova, K.T., Dobretsov, N.L., 1991. Metamorphic formations of Tajikistan. Donish, Dushanbe.
- Burtman, V.S., Molnar, P., 1993. Geological and Geophysical Evidence for Deep Subduction of Continental Crust Beneath the Pamir, in: *Geological Society of America Special Papers*. Geological Society of America, pp. 1–76. <https://doi.org/10.1130/SPE281-p1>
- Carmichael, C.M., 1961. The magnetic properties of ilmenite-haematite crystals. *Proc. R. Soc. Lond. Ser. Math. Phys. Sci.* 263, 508–530. <https://doi.org/10.1098/rspa.1961.0177>
- Chapman, J.B., Carrapa, B., Ballato, P., Decelles, P.G., Worthington, J., Oimahmadov, I., Tre, R., 2017. Intracontinental Subduction beneath the Pamir Mountains: Constraints from Thermokinematic Modeling of Shortening in the Tajik Fold-and-Thrust Belt. *GSA Bulletin* 129, 1–22.
- Chapman, J.B., Scoggin, S.H., Kapp, P., Carrapa, B., Ducea, M.N., Worthington, J., Oimahmadov, I., Gadoev, M., 2018a. Mesozoic to Cenozoic magmatic history of the Pamir. *Earth Planet. Sci. Lett.* 482, 181–192. <https://doi.org/10.1016/j.epsl.2017.10.041>
- Chapman, J.B., Robinson, A.C., Carrapa, B., Villarreal, D., Worthington, J., DeCelles, P.G., Kapp, P., Gadoev, M., Oimahmadov, I., Gehrels, G., 2018b; Cretaceous shortening and exhumation history of the South Pamir terrane. *Lithosphere* 10 (4), 494–511. <https://doi.org/10.1130/L691.1>

- Coney, P. J., & Harms, T. A., 1984. Cordilleran metamorphic core complexes—Cenozoic extensional relics of Mesozoic compression. *Geology*, 12(9), 550–554. [https://doi.org/10.1130/0091-7613\(1984\)12<550:Cmcce>2.0.Co;2](https://doi.org/10.1130/0091-7613(1984)12<550:Cmcce>2.0.Co;2)
- de Sigoyer, J., Guillot, S., Dick, P., 2004. Exhumation of the ultrahigh-pressure Tso Moriri unit in eastern Ladakh (NW Himalaya): A case study. *Tectonics* 23, TC3003. <https://doi.org/10.1029/2002TC001492>
- Dronov, V.I., Budanov, V.I., Volkova, N.I., 1994. Stratigraphy of the Paleocene volcanic and sedimentary deposits of lower reaches of the Bartang River (Central Pamir, Nakhchipat - Kudara zone). *Izv. Akad. Nauk Resp. Tajikistan* 30–36.
- Fodor, R.V., Stoddard, E.F., Burt, E.R., 1981. Origin of spessartine-rich garnet in meta-rhyolite, Carolina slate belt. *Southeast. Geol.* 22, 103–114.
- Fuller, M.D., 1963. Magnetic anisotropy and paleomagnetism. *J. Geophys. Res.* 68, 293–309. <https://doi.org/10.1029/JZ068i001p00293>
- Grew, E., Pertsev, N.N., Yates, M.G., Christy, A.G., Marquez, N., Chernosky, J.V., 1994. Sapphirine+Forsterite and Sapphirine+Humite-Group Minerals in an Ultra-Magnesian Lens from Kuhl-i-lal, SW Pamirs, Tajikistan: Are these Assemblages Forbidden? *J. Petrol.* 35, 1275–1293. <https://doi.org/10.1093/petrology/35.5.1275>
- Hacker, B.R., Ratschbacher, L., Rutte, D., Stearns, M.A., Malz, N., Stübner, K., Kylander-Clark, A.R.C., Pfänder, J.A., Everson, A., 2017. Building the Pamir-Tibet Plateau—Crustal stacking, extensional collapse, and lateral extrusion in the Pamir: 3. Thermobarometry and petrochronology of deep Asian crust. *Tectonics* 36, 1743–1766. <https://doi.org/10.1002/2017TC004488>
- Halama, R., Konrad-Schmolke, M., Sudo, M., Marschall, H.R., Wiedenbeck, M., 2014. Effects of fluid–rock interaction on ⁴⁰Ar/³⁹Ar geochronology in high-pressure rocks (Sesia-Lanzo Zone, Western Alps). *Geochim. Cosmochim. Acta* 126, 475–494. <https://doi.org/10.1016/j.gca.2013.10.023>
- Henry, B., Jordanova, D., Jordanova, N., Souque, C., Robion, P., 2003. Anisotropy of magnetic susceptibility of heated rocks. *Tectonophysics* 366, 241–258. [https://doi.org/10.1016/S0040-1951\(03\)00099-4](https://doi.org/10.1016/S0040-1951(03)00099-4)
- Horton, F., Lee, J., Hacker, B., Bowman-Kamaha'o, M., Cosca, M., 2015. Himalayan gneiss dome formation in the middle crust and exhumation by normal faulting: New geochronology of Gianbul dome, northwestern India. *GSA Bulletin* 127, 162–180. <https://doi.org/10.1130/B31005.1>
- Hunt, C.P., Moskowitz, B.M., Banerjee, S.K., 1995. Magnetic Properties of Rocks and Minerals, in: Ahrens, T.J. (Ed.), *AGU Reference Shelf. American Geophysical Union, Washington, D. C.*, pp. 189–204. <https://doi.org/10.1029/RF003p0189>
- Jelinek, V., 1981. Characterization of the magnetic fabric of rocks. *Tectonophysics* 79, T63–T67. [https://doi.org/10.1016/0040-1951\(81\)90110-4](https://doi.org/10.1016/0040-1951(81)90110-4)
- Imrecke, D., B., Robinson, A.C., Owen, L.A., Chen, J., Schoenbohm, L.M., Hedrick, K.A., Lapen, T.J., Li, W., Yuan, Z., 2019. Mesozoic Evolution of the Eastern Pamir. *Lithosphere* 11(4), 560–80. <https://doi.org/10.1130/L1017.1>
- Kufner, S.-K., Schurr, B., Ratschbacher, L., Murodkulov, S., Abdulhameed, S., Ischuk, A., et al., 2018. Seismotectonics of the Tajik basin and surrounding mountain ranges. *Tectonics*, 37, 2404–2424. <https://doi.org/10.1029/2017TC004812>
- Lanci, L., 2010. Detection of Multi-Axial Magnetite by Remanence Effect on Anisotropy of Magnetic Susceptibility. *Geophys. J. Int.*, 181, 1362–1366. <https://doi.org/10.1111/j.1365-246X.2010.04588.x>.
- Laskowski, A.K., Kapp, P., Ding, L., Campbell, C., Liu, X., 2017. Tectonic evolution of the Yarlung suture zone, Lopu Range region, southern Tibet. *Tectonics* 36, 108–136. <https://doi.org/10.1002/2016TC004334>

- Lee, J., Hacker, B., Wang, Y., 2004. Evolution of North Himalayan gneiss domes: structural and metamorphic studies in Mabja Dome, southern Tibet. *Journal of Structural Geology* 26, 2297–2316. <https://doi.org/10.1016/j.jsg.2004.02.013>
- Li, Y.-P., Robinson, A.C., Gadoev, M. and Oimhammadzoda, I., 2020a. Was the Pamir salient built along a Late Paleozoic embayment on the southern Asian margin?. *Earth and Planetary Science Letters*, 550, p.116554.
- Li, Y.-P., Robinson, A.C., Lapen, T.J., Richter, M., Stevens, M.K., 2020b. Muztaghata Dome Miocene Eclogite Facies Metamorphism: A Record of Lower Crustal Evolution of the NE Pamir. *Tectonics* 39, e2019TC005917. <https://doi.org/10.1029/2019TC005917>
- Lukens, C.E., Carrapa, B., Singer, B.S., Gehrels, G., 2012. Miocene exhumation of the Pamir revealed by detrital geothermochronology of Tajik rivers. *Tectonics* 31. <https://doi.org/10.1029/2011TC003040>
- Martin-Hernandez, F., Hirt, A.M., 2003. The anisotropy of magnetic susceptibility in biotite, muscovite and chlorite single crystals. *Tectonophysics* 367, 13–28.
- McEnroe, S.A., Brown, L.L., 2000. A closer look at remanence-dominated aeromagnetic anomalies: rock magnetic properties and magnetic mineralogy of the Russell Belt microcline-sillimanite gneiss, northwest Adirondack Mountains, New York. *J. Geophys. Res.* 105, 16437–56.
- McEnroe, S.A., Fabian, K., Robinson, P., Gaina, C., Brown, L.L., 2009. Crustal Magnetism, Lamellar Magnetism and Rocks That Remember. *Elements* 5, 241–246.
- McEnroe, S.A., Harrison, R.J., Robinson, P., Golla, U., Jercinovic, M.J., 2001. Effect of fine-scale microstructures in titanohematite on the acquisition and stability of natural remanent magnetization in granulite facies metamorphic rocks, southwest Sweden: Implications for crustal magnetism. *J. Geophys. Res. Solid Earth* 106, 30523–30546. <https://doi.org/10.1029/2001JB000180>
- Merrill, R.T., Grommé, C.S., 1969. Nonreproducible self-reversal of magnetization in diorite. *J. Geophys. Res.* 1896-1977 74, 2014–2024. <https://doi.org/10.1029/JB074i008p02014>
- Murphy, M.A., Yin, A., Kapp, P., Harrison, T.M., Manning, C.E., Ryerson, F.J., Lin, D., Jinghui, G., 2002. Structural evolution of the Gurla Mandhata detachment system, southwest Tibet: Implications for the eastward extent of the Karakoram fault system. *GSA Bulletin* 114, 428–447. [https://doi.org/10.1130/0016-7606\(2002\)114<0428:SEOTGM>2.0.CO;2](https://doi.org/10.1130/0016-7606(2002)114<0428:SEOTGM>2.0.CO;2)
- Nagata, T., Uyeda, S., 1959. Exchange Interaction as a Cause of Reverse Thermo-Remanent Magnetism. *Nature* 184, 890–891. <https://doi.org/10.1038/184890a0>
- Pashkov, B., Shvolman, V., 1979. Rift margins of Tethys in the Pamirs. *Geotectonics* 13, 447–456.
- Potter, D.K., Stephenson, A., 1990a. Field-impressed anisotropies of magnetic susceptibility and remanence in minerals. *J. Geophys. Res. Solid Earth* 95, 15573–15588. <https://doi.org/10.1029/JB095iB10p15573>
- Puzankov, Y.M., Anoshin, G.N., Budanov, V.I., Volynets, O.N., Melgunov, S.V., 2000. Meso-Cenozoic collision-accretionary volcanic complexes of the Central and Southern Pamirs (an example of active margin-plume magmatism evolution). *Russ. Geol. Geophys.* 41, 616–632.
- Ratschbacher, L., Frisch, W., Neubauer, F., Schmid, S.M., Neugebauer, J., 1989. Extension in compressional orogenic belts: The eastern Alps. *Geology* 17, 404–407. [https://doi.org/10.1130/0091-7613\(1989\)017<0404:EICOBT>2.3.CO;2](https://doi.org/10.1130/0091-7613(1989)017<0404:EICOBT>2.3.CO;2)
- Rembe, J., Sobel, E.R., Kley, J., Zhou, R., Thiede, R., Chen, J., 2021. The Carboniferous Arc of the North Pamir. *Lithosphere* 2021, 6697858. <https://doi.org/10.2113/2021/6697858>
- Rembe, J., Zhou, R., Sobel, E.R., Kley, J., Chen, J., Zhao, J.-X., Feng, Y., Howard, D.L., 2022. Calcite U–Pb dating of altered ancient oceanic crust in the North Pamir, Central Asia. *Geochronology* 4, 227–250. <https://doi.org/10.5194/gchron-4-227-2022>

- Robinson, A.C., 2015. Mesozoic tectonics of the Gondwanan terranes of the Pamir plateau. *J. Asian Earth Sci.*, Special Issue on Cimmerian Terranes 102, 170–179. <https://doi.org/10.1016/j.jseaes.2014.09.012>
- Robinson, P., Harrison, R.J., McEnroe, S.A., Hargraves, R.B., 2002. Lamellar magnetism in the haematite–ilmenite series as an explanation for strong remanent magnetization. *Nature* 418, 517–520. <https://doi.org/10.1038/nature00942>
- Rochette, P., Jackson, M., Aubourg, C., 1992. Rock magnetism and the interpretation of anisotropy of magnetic susceptibility. *Rev. Geophys.* 30, 209–226. <https://doi.org/10.1029/92RG00733>
- Roperch, P., Carlotto, V., Chauvin, A., 2010. Using anisotropy of magnetic susceptibility to better constrain the tilt correction in paleomagnetism: A case study from southern Peru. *Tectonics* 29, TC6005. <https://doi.org/10.1029/2009TC002639>
- Roperch, P., Kissel, C., Lagroix, F., Dupont-Nivet, G., Chauvin, A., Poblete, F., Aminov, J., submitted. Anisotropy of magnetic susceptibility impressed during rock magnetic procedures (AF, IRM) and information on the domain state of the magnetic carriers. *Physics of the Earth & Planetary Interiors*.
- Ruffet, G., Féraud, G., Amouric, M., 1991. Comparison of ^{40}Ar - ^{39}Ar conventional and laser dating of biotites from the North Trégor Batholith. *Geochim. Cosmochim. Acta* 55, 1675–1688. [https://doi.org/10.1016/0016-7037\(91\)90138-U](https://doi.org/10.1016/0016-7037(91)90138-U)
- Ruffet, G., Féraud, G., Balèvre, M., Kiénaast, J.-R., 1995. Plateau ages and excess argon in phengites: an ^{40}Ar - ^{39}Ar laser probe study of Alpine micas (Sesia Zone, Western Alps, northern Italy). *Chem. Geol.* 121, 327–343. [https://doi.org/10.1016/0009-2541\(94\)00132-R](https://doi.org/10.1016/0009-2541(94)00132-R)
- Rutte, D., Ratschbacher, L., Khan, J., Stübner, K., Hacker, B.R., Stearns, M.A., Enkelmann, E., Jonckheere, R., Pfänder, J.A., Sperner, B., Tichomirowa, M., 2017a. Building the Pamir-Tibetan Plateau—Crustal stacking, extensional collapse, and lateral extrusion in the Central Pamir: 2. Timing and rates. *Tectonics* 36, 385–419. <https://doi.org/10.1002/2016TC004294>
- Rutte, D., Ratschbacher, L., Schneider, S., Stübner, K., Stearns, M.A., Gulzar, M.A., Hacker, B.R., 2017b. Building the Pamir-Tibetan Plateau—Crustal stacking, extensional collapse, and lateral extrusion in the Central Pamir: 1. Geometry and kinematics. *Tectonics* 36, 342–384. <https://doi.org/10.1002/2016TC004293>
- Schmidt, J., Hacker, B.R., Ratschbacher, L., Stübner, K., Stearns, M., Kylander-Clark, A., Cottle, J.M., Alexander, A., Webb, G., Gehrels, G., Minaev, V., 2011. Cenozoic deep crust in the Pamir. *Earth Planet. Sci. Lett.* 312, 411–421. <https://doi.org/10.1016/j.epsl.2011.10.034>
- Schmidt, V.A., Fuller, M.D., 1970. Low Field Susceptibility Anisotropy in the Basal Plane of Hematite ($\alpha\text{-Fe}_2\text{O}_3$) and its Dependence on the Remanent Moment. *J. Appl. Phys.* 41, 994–995. <https://doi.org/10.1063/1.1659050>
- Shvolman, V., 1980. A mesozoic ophiolite complex in the Pamirs. *Geotectonics* 14, 465–470.
- Schwab, M., Ratschbacher, L., Siebel, W., McWilliams, M., Minaev, V., Lutkov, V., Chen, F., Stanek, K., Nelson, B., Frisch, W., Wooden, J.L., 2004. Assembly of the Pamirs: Age and origin of magmatic belts from the southern Tien Shan to the southern Pamirs and their relation to Tibet. *Tectonics* 23, n/a-n/a. <https://doi.org/10.1029/2003TC001583>
- Searle, M.P., Lamont, T.N., 2019. Compressional metamorphic core complexes, low-angle normal faults and extensional fabrics in compressional tectonic settings. *Geol. Mag.* 1–18. <https://doi.org/10.1017/S0016756819000207>
- Spear, F.S., 1994. Metamorphic Phase Equilibria and Pressure—Temperature—Time Paths. *Geol. Mag.* 131, 799p. <https://doi.org/10.1017/S0016756800012486>
- Stearns, M.A., Hacker, B.R., Ratschbacher, L., Rutte, D., Kylander-Clark, A.R.C., 2015. Titanite petrochronology of the Pamir gneiss domes: Implications for middle to deep crust exhumation and

- titanite closure to Pb and Zr diffusion. *Tectonics* 34, 784–802. <https://doi.org/10.1002/2014TC003774>
- Stübner, K., Ratschbacher, L., Rutte, D., Stanek, K., Minaev, V., Wiesinger, M., Gloaguen, R., 2013a. The giant Shakh dara migmatitic gneiss dome, Pamir, India-Asia collision zone: 1. Geometry and kinematics. *Tectonics* 32, 948–979. <https://doi.org/10.1002/tect.20057>
- Stübner, K., Ratschbacher, L., Weise, C., Chow, J., Hofmann, J., Khan, J., Rutte, D., Sperner, B., Pfänder, J.A., Hacker, B.R., Dunkl, I., Tichomirowa, M., Stearns, M.A., 2013b. The giant Shakh dara migmatitic gneiss dome, Pamir, India-Asia collision zone: 2. Timing of dome formation. *Tectonics* 32, 1404–1431. <https://doi.org/10.1002/tect.20059>
- Tajidinov, K.S., 1968. Volcano-plutonic complex of rocks of the Bartang-Pshart zone of the Central Pamir (Doctoral dissertation). Institute of Geology of the Academy of Sciences of the Tajik SSR, Dushanbe, Tajikistan.
- Tirel, C., Brun, J.-P., and Burov, E., 2004, Thermomechanical modeling of extensional gneiss domes, in Whitney, D.L., Teyssier, C., and Siddoway, C.S., Gneiss domes in orogeny: Boulder, Colorado, Geological Society of America Special Paper 380, p. 67–78. <https://doi.org/10.1130/0-8137-2380-9.67>
- Verdel, C., Wernicke, B.P., Ramezani, J., Hassanzadeh, J., Renne, P.R., Spell, T.L., 2007. Geology and thermochronology of Tertiary Cordilleran-style metamorphic core complexes in the Saghand region of central Iran. *GSA Bulletin* 119, 961–977. <https://doi.org/10.1130/B26102.1>
- Vlasov, N.G., Dyakov, Y.A., Cherev, E.S., 1991. Geological map of the Tajik SSR and adjacent territories, 1: 500,000.
- Waldhör, M., Appel, E., Frisch, W., Patzelt, A., 2001. Palaeomagnetic investigation in the Pamirs and its tectonic implications. *J. Asian Earth Sci.* 19, 429–451. [https://doi.org/10.1016/S1367-9120\(00\)00030-4](https://doi.org/10.1016/S1367-9120(00)00030-4)
- Whitney, D.L., Teyssier, C., and Vanderhaeghe, O., 2004. Gneiss domes and crustal flow, in Whitney, D.L., Teyssier, C., and Siddoway, C.S., Gneiss domes in orogeny: Boulder, Colorado, Geological Society of America Special Paper 380, p. 15–33. <https://doi.org/10.1130/0-8137-2380-9.15>
- Whitney, D.L., Evans, B.W., 2010. Abbreviations for names of rock-forming minerals. *Am. Mineral.* 95, 185–187. <https://doi.org/10.2138/am.2010.3371>
- Wilke, F.D.H., O'Brien, P.J., Gerdes, A., Timmerman, M.J., Sudo, M., Ahmed Khan, M., 2010. The multistage exhumation history of the Kaghan Valley UHP series, NW Himalaya, Pakistan from U-Pb and $40\text{Ar}/39\text{Ar}$ ages. *Eur. J. Mineral.* 22, 703–719. <https://doi.org/10.1127/0935-1221/2010/0022-2051>
- Worthington, J.R., Ratschbacher, L., Stübner, K., Khan, J., Malz, N., Schneider, S., Kapp, P., Chapman, J.B., Goddard, A.S., Brooks, H.L., Lamadrid, H.M., Steele-MacInnis, M., Rutte, D., Jonckheere, R., Pfänder, J., Hacker, B.R., Oimahmadov, I., Gadoev, M., 2020. The Alichur Dome, South Pamir, Western India–Asia Collisional Zone: Detailing the Neogene Shakh dara–Alichur Syn-collisional Gneiss-Dome Complex and Connection to Lithospheric Processes. *Tectonics* 39, e2019TC005735. <https://doi.org/10.1029/2019TC005735>
- Yin, A., 2004. Gneiss domes and gneiss dome systems, in Whitney, D.L., Teyssier, C., and Siddoway, C.S., eds., Gneiss domes in orogeny: Boulder, Colorado, Geological Society of America Special Paper 380, p. 1–14. <https://doi.org/10.1130/0-8137-2380-9.1>
- Zapletal, K., Kropáček, V., 1985. Magnetic anisotropy of polycrystalline haematite induced by a DC magnetic field. *Stud. Geophys. Geod.* 29, 351–361.
- Zhou, Y., He, J., Oimahmadov, I., Gadoev, M., Pan, Z., Wang, W., Abdulov S. & Rajabov, N., 2016. Present-day crustal motion around the Pamir Plateau from GPS measurements. *Gondwana Research*, 35, 144–154. <https://doi.org/10.1016/j.gr.2016.03.011>

Supplementary information : Analytical methods

1.0 $^{40}\text{Ar}/^{39}\text{Ar}$ and Rb/Sr thermochronology :

1.1 $^{40}\text{Ar}/^{39}\text{Ar}$ Potsdam Laboratory

The dating system and the common procedure for $^{40}\text{Ar}/^{39}\text{Ar}$ dating has been described in Wilke et al. (2010) and Halama et al. (2014), but the summary of the procedure is as follows. Neutron activation of the samples was performed at CLICIT (Cadmium-Lined in-Core Irradiation Tube) facility of Oregon State TRIGA Reactor (OSTR), USA. The unknown samples, the neutron flux monitoring mineral, Fish Canyon Tuff sanidine, FCs-EK, (28.294 Ma, Renne et al., 2010; 2011) prepared by Scottish Universities Environmental Research Centre (SUERC) (Morgan et al., 2014) in University of Glasgow, UK, and crystals of K_2SO_4 and CaF_2 for correction of interference by the other Ar isotopes produced by K and Ca in samples were wrapped by commercial Al foils, then contained into the 99.999% pure Al sample container with the column shape of 22.7 mm diameter and 101.5 mm height in total. The Cd-tube of the CLICIT facility contributes to cut off the thermal neutron flux to reduce unnecessary nuclear reactions within the samples. All samples were irradiated for 4 hours with the fast neutron flux of $2.5 \times 10^{13} \text{ n/cm}^2/\text{s}$. After cooling samples for a few weeks at the reactor, they were sent back to Potsdam where Ar isotopic analyses were conducted.

The gas extracted with a CO_2 laser from a few biotite grains was introduced into an ultra-high vacuum purification-line and was held for 10 minutes to purify the gas to pure Ar. Thereafter, the argon isotopic ratios were determined with the Micromass 5400a noble gas mass spectrometer. All Ar isotope ratios were finally obtained after blank, mass discrimination, interference and decay corrections. Each J value at one location was obtained as a weighted or arithmetic mean of four single grain total fusion analyses of the Fish Canyon Tuff sanidine grains. Then the J values of the unknown samples were interpolated from these directly obtained J values. The valve operations of the analytical system, $^{40}\text{Ar}/^{39}\text{Ar}$ age and isochron calculation were conducted by Mass Spec software of Dr. Alan Deino from Berkeley Geochronology Center, USA. The atmospheric $^{40}\text{Ar}/^{36}\text{Ar}$ ratio of 298.56 was used (Lee et al., 2006), as was the decay constants for ^{40}K of Renne et al. (2010; 2011). Our used interference correction parameters are: $(^{39}\text{Ar}/^{37}\text{Ar})_{\text{Ca}} = (6.64 \pm 0.26) \times 10^{-4}$, $(^{36}\text{Ar}/^{37}\text{Ar})_{\text{Ca}} = (2.73 \pm 0.03) \times$

10^{-4} , $(^{40}\text{Ar}/^{39}\text{Ar})_{\text{K}} = (51 \pm 24) \times 10^{-4}$ and $(^{38}\text{Ar}/^{39}\text{Ar})_{\text{K}} = (1.182 \pm 0.003) \times 10^{-2}$. Plateau age definitions are those of Fleck et al. (1977). All errors (in the figures and tables) indicate 1 sigma analytical uncertainty.

1.2 $^{40}\text{Ar}/^{39}\text{Ar}$ Géosciences Rennes laboratory

The whole-rock millimetric fragment was step-heated with a CO_2 (Synrad®) laser probe, following the procedures described in Ruffet et al. (1991, 1995).

Its Irradiation was performed at McMaster Nuclear Reactor (Canada) in the 8C facility and lasted 66.667 h with an efficiency (J/h) of $9.928 \times 10^{-5} \text{ h}^{-1}$. The irradiation standard was sanidine TCRs ($28.608 \pm 0.033 \text{ Ma}$; Renne *et al.*, 1998, 2010 and 2011). Blanks were performed routinely each first or third/fourth run, and were subtracted from the subsequent sample gas fractions. Apparent age errors are at the 1σ level (Fig.4). They do not include errors on the $^{40}\text{Ar}^*/^{39}\text{Ar}_{\text{K}}$ ratio and age of the monitor and decay constants. These errors are, however, included in the final calculation of the error (1σ) of the plateau age. Analytical data and parameters used for calculations, such as isotopic ratios measured on pure K and Ca salts; mass discrimination; atmospheric argon ratios; J parameter; decay constants are in the electronic supplementary data material.

1.3 Rb/Sr dating (Potsdam laboratory)

The measurement of the Sr isotopic composition was performed in dynamic multicollection mode, whereas Rb isotope dilution was done in static multicollection mode. The $^{87}\text{Sr}/^{86}\text{Sr}$ value of 0.710242 ± 0.000020 (2σ , $n=16$) was obtained for the NIST SRM 987 isotopic standard during the period of analytical work. In order to calculate the age, we assigned standard uncertainties of $\pm 0.005\%$ for $^{87}\text{Sr}/^{86}\text{Sr}$ and of $\pm 1.5\%$ for $^{87}\text{Rb}/^{86}\text{Sr}$ ratios to the results. Individual analytical uncertainties were generally smaller than these values. The reader is referred to Glodny et al. (2008) for the more detailed description of handling the mineral separates and the analytical procedures. The Rb-Sr isotope and age data uncertainties are quoted at 2σ . Regression lines were calculated using the ISOPLOT program of Ludwig (2009). The ^{87}Rb decay constant recommended by Villa et al. (2015) was used.

2.0 Paleomagnetic methods

The stepwise alternating field (AF) demagnetization using the 2G AF static demagnetizer was inefficient to demagnetize these samples because of their high magnetic coercivity. All samples (one specimen per core) were thus progressively thermally demagnetized in an MMTD furnace, in which the residual field was less than 10 nT. To monitor any eventual heating-induced magnetic mineralogical changes, we measured the samples' magnetic susceptibility after each thermal demagnetization step. Acquisition of isothermal remanent magnetization (IRM) and subsequent thermal demagnetization were investigated in order to identify the carriers of the ChRM. IRM was applied with an ASC Scientific pulse electromagnet. The magnetic minerals and the amount of rock mineral alteration that could affect their magnetic record were also investigated by the means of petrographic microscopy and a scanning electron microscope. To this end, polished thin-sections were investigated under a petrographic microscope in transmitted and reflected light, after which they were scanned with a scanning electron microscope (SEM) equipped with an energy dispersive X-ray spectrometer (EDS). Anisotropy of magnetic susceptibility (AMS) was measured with the KLY3 Agico spinner kappabridge. Low field magnetic susceptibility with temperature (K/T) was measured with the Agico KLY3/CS3 apparatus. Hysteresis cycles were measured with AGM and VSM instruments at LSCE (Gif/Yvette, France). Low temperature experiments were carried out with a magnetometer MPMS XL5 at IPGP.

References:

- Fleck, R.J., Sutter, J.F., Elliot, D.H., 1977. Interpretation of discordant $^{40}\text{Ar}/^{39}\text{Ar}$ age-spectra of mesozoic tholeiites from antarctica. *Geochim. Cosmochim. Acta* 41, 15–32. [https://doi.org/10.1016/0016-7037\(77\)90184-3](https://doi.org/10.1016/0016-7037(77)90184-3)
- Glodny, J., Ring, U., Kühn, A., 2008. Coeval high-pressure metamorphism, thrusting, strike-slip, and extensional shearing in the Tauern Window, Eastern Alps. *Tectonics* 27. <https://doi.org/10.1029/2007TC002193>
- Halama, R., Konrad-Schmolke, M., Sudo, M., Marschall, H.R., Wiedenbeck, M., 2014. Effects of fluid–rock interaction on $^{40}\text{Ar}/^{39}\text{Ar}$ geochronology in high-pressure rocks (Sesia-Lanzo Zone, Western Alps). *Geochim. Cosmochim. Acta* 126, 475–494. <https://doi.org/10.1016/j.gca.2013.10.023>
- Lee, J.-Y., Marti, K., Severinghaus, J.P., Kawamura, K., Yoo, H.-S., Lee, J.B., Kim, J.S., 2006. A redetermination of the isotopic abundances of atmospheric Ar. *Geochim. Cosmochim. Acta* 70, 4507–4512. <https://doi.org/10.1016/j.gca.2006.06.1563>
- Ludwig, K.R., 2009. Isoplot/Ex Ver 3.71: A Geochronological Toolkit For Microsoft Excel.
- Morgan, L.E., Mark, D.F., Imlach, J., Barfod, D., Dymock, R., 2014. FCs-EK: a new sampling of the Fish Canyon Tuff $^{40}\text{Ar}/^{39}\text{Ar}$ neutron flux monitor. *Geol. Soc. Lond. Spec. Publ.* 378, 63–67. <https://doi.org/10.1144/SP378.21>
- Renne, P.R., Swisher, C.C., Deino, A.L., Karner, D.B., Owens, T.L., DePaolo, D.J., 1998. Intercalibration of standards, absolute ages and uncertainties in $^{40}\text{Ar}/^{39}\text{Ar}$ dating. *Chem. Geol.* 145, 117–152. [https://doi.org/10.1016/S0009-2541\(97\)00159-9](https://doi.org/10.1016/S0009-2541(97)00159-9)

- Renne, P.R., Balco, G., Ludwig, K.R., Mundil, R., Min, K., 2011. Response to the comment by W.H. Schwarz et al. on “Joint determination of 40K decay constants and 40Ar*/40K for the Fish Canyon sanidine standard, and improved accuracy for 40Ar/39Ar geochronology” by P.R. Renne et al. (2010). *Geochim. Cosmochim. Acta* 75, 5097–5100. <https://doi.org/10.1016/j.gca.2011.06.021>
- Renne, P.R., Mundil, R., Balco, G., Min, K., Ludwig, K.R., 2010. Joint determination of 40K decay constants and 40Ar*/40K for the Fish Canyon sanidine standard, and improved accuracy for 40Ar/39Ar geochronology. *Geochim. Cosmochim. Acta* 74, 5349–5367. <https://doi.org/10.1016/j.gca.2010.06.017>
- Villa, I.M., De Bièvre, P., Holden, N.E., Renne, P.R., 2015. IUPAC-IUGS recommendation on the half life of 87Rb. *Geochim. Cosmochim. Acta* 164, 382–385. <https://doi.org/10.1016/j.gca.2015.05.025>
- Wilke, F.D.H., O’Brien, P.J., Gerdes, A., Timmerman, M.J., Sudo, M., Ahmed Khan, M., 2010. The multistage exhumation history of the Kaghan Valley UHP series, NW Himalaya, Pakistan from U-Pb and 40Ar/39Ar ages. *Eur. J. Mineral.* 22, 703–719. <https://doi.org/10.1127/0935-1221/2010/0022-2051>

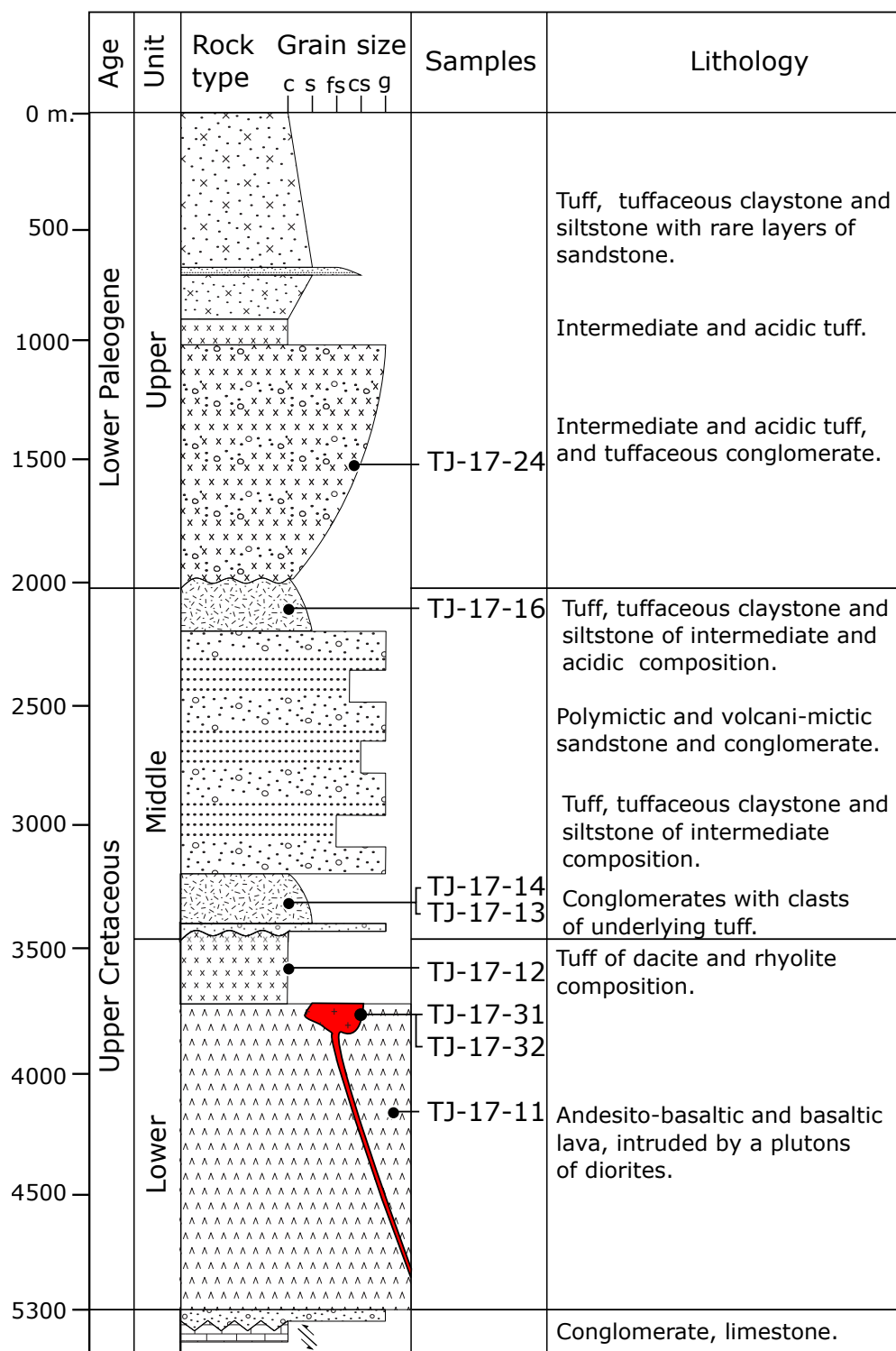


Fig. S1. Stratigraphic log of the Bartang volcanic and volcanoclastic sequence. Sketched based on our observations and observations of Dronov (1994). See the text for the reference.

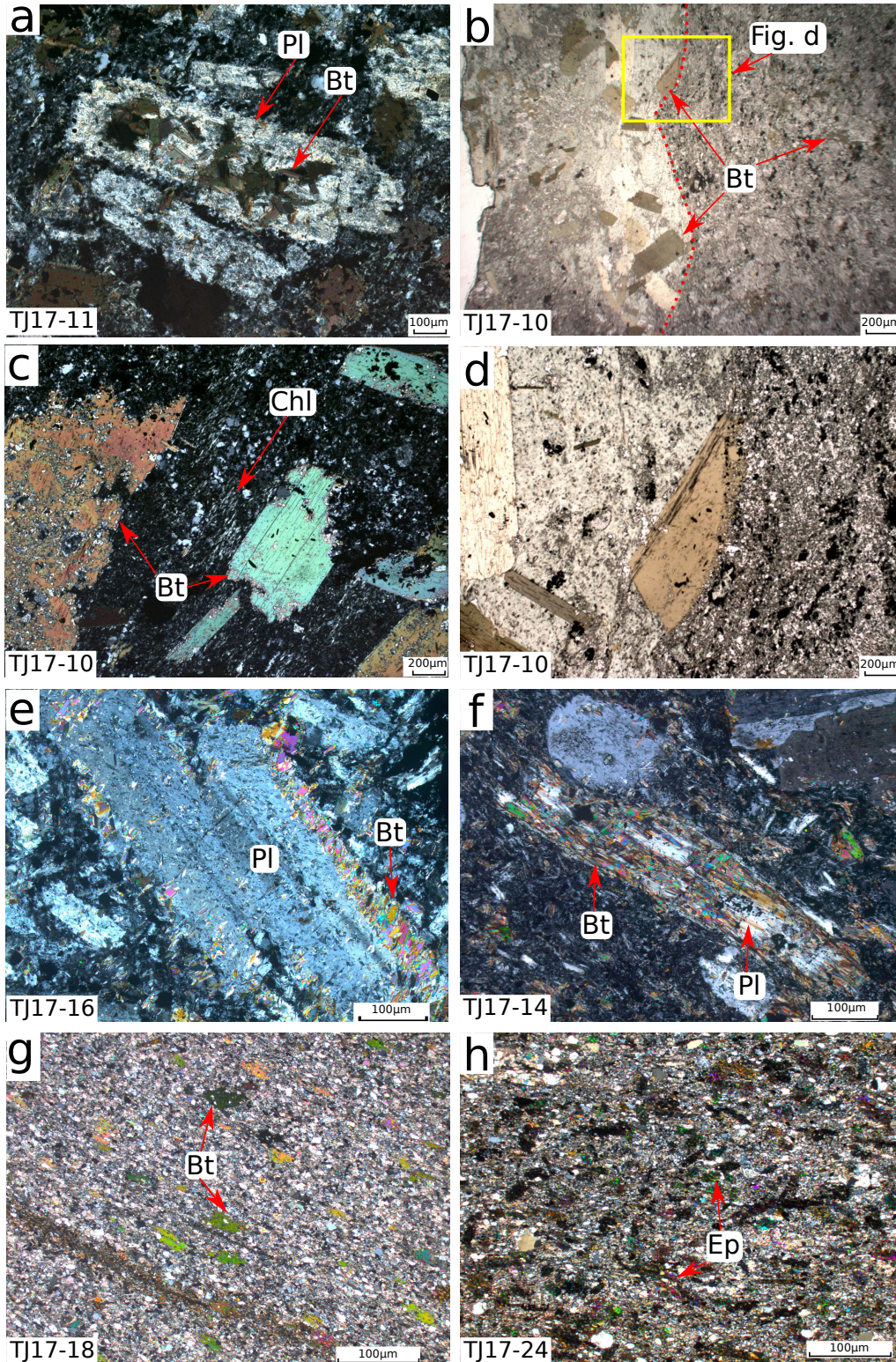


Fig. S2. Photomicrographs of petrographic thin-sections. See the text for description of slides. Pl - plagioclase, Bt - biotite, Ep - epidote, Cal - calcite.

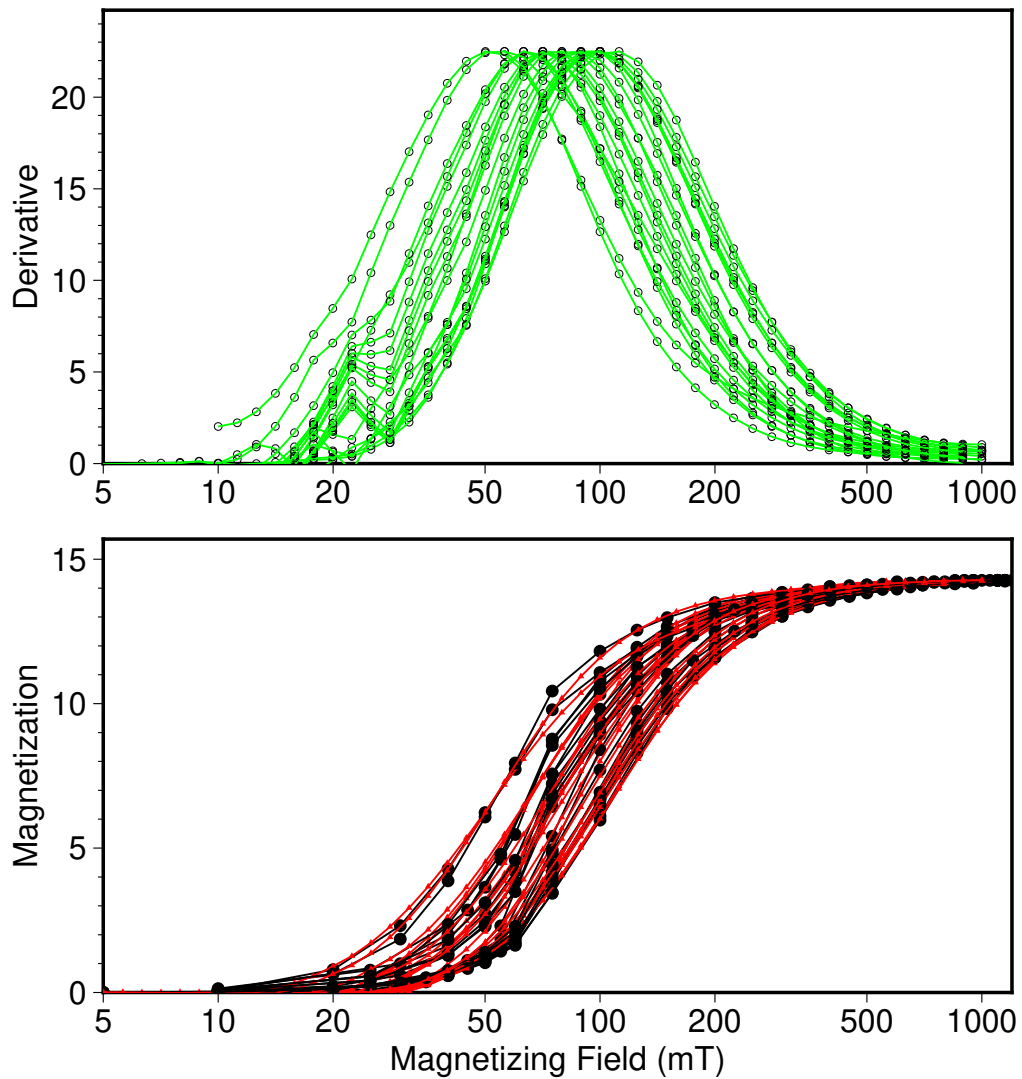


Figure S3. Isothermal remanent magnetization (IRM) acquisition in Log scale (bottom) and related first derivatives (top). The derivative is calculated from the interpolated data (red curve).

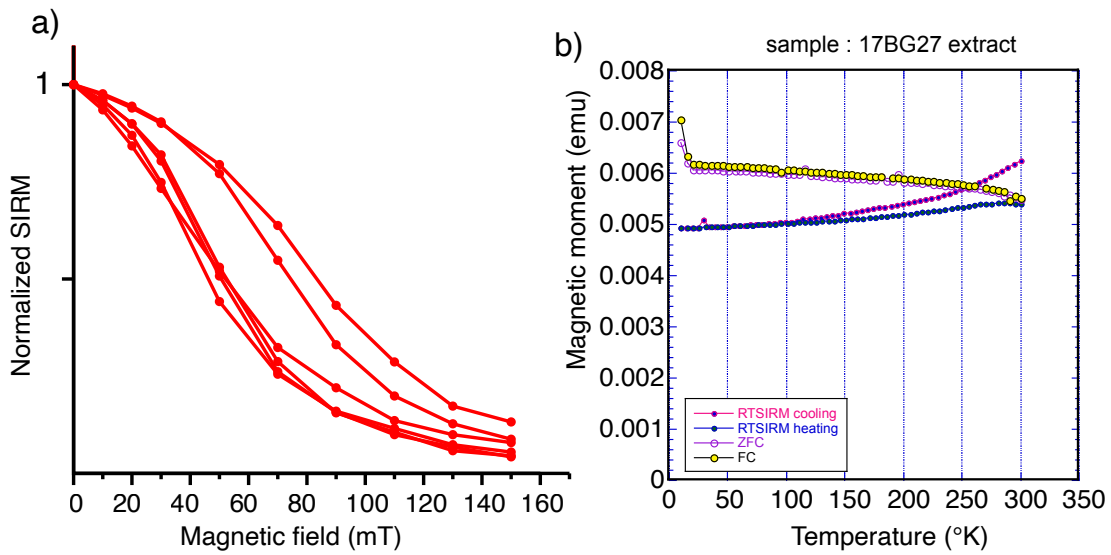


Figure S4. a) Alternating field demagnetization of IRM acquired at 1 tesla; b) Low temperature measurements with the MPMS XL5 magnetometer for one sample of volcanoclastic sediments (manual magnetic extracts). RTSIRM: room temperature saturation IRM; ZFC/FC are the zero field cooled and field cooled data.

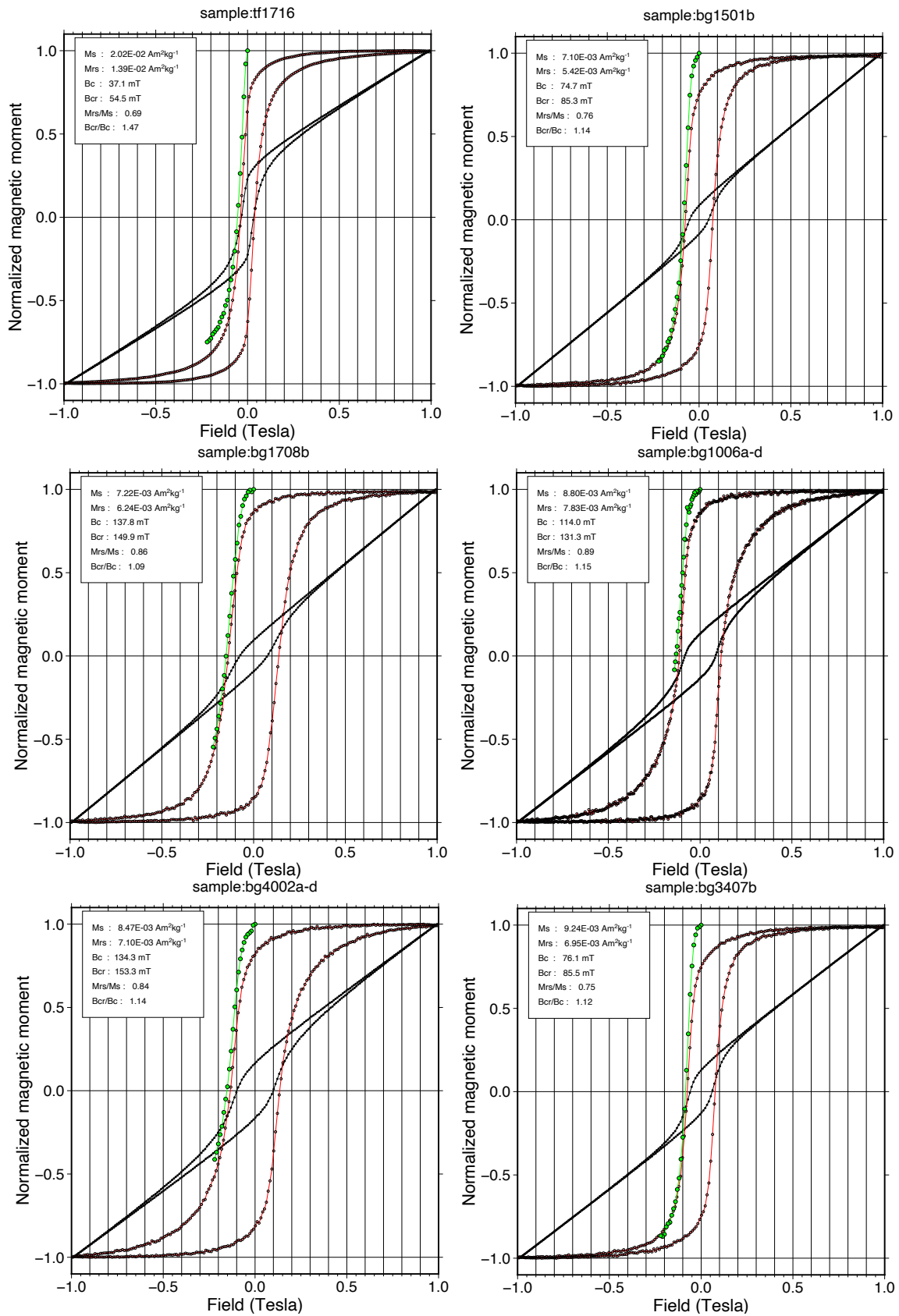


Figure S5. Examples of hysteresis cycles for six samples from Bartang. The red curve is after correction for paramagnetism. The samples are characterized by high Mrs/Ms ratio and low values of Bcr/Bc.

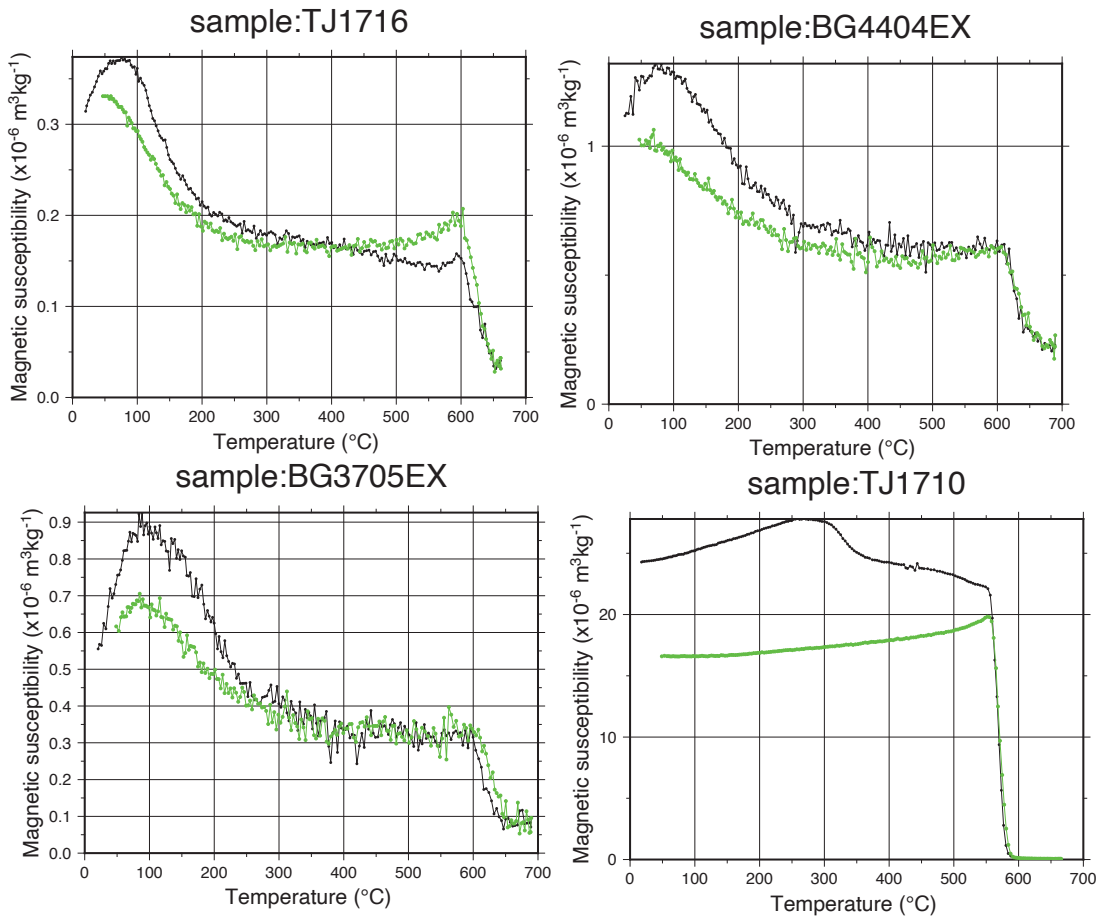


Figure S6. Variation of the magnetic susceptibility as a function of the temperature measured with the Agico Kappabridge KLY3-CS3 system. Heating/ cooling curves in black/green color respectively.

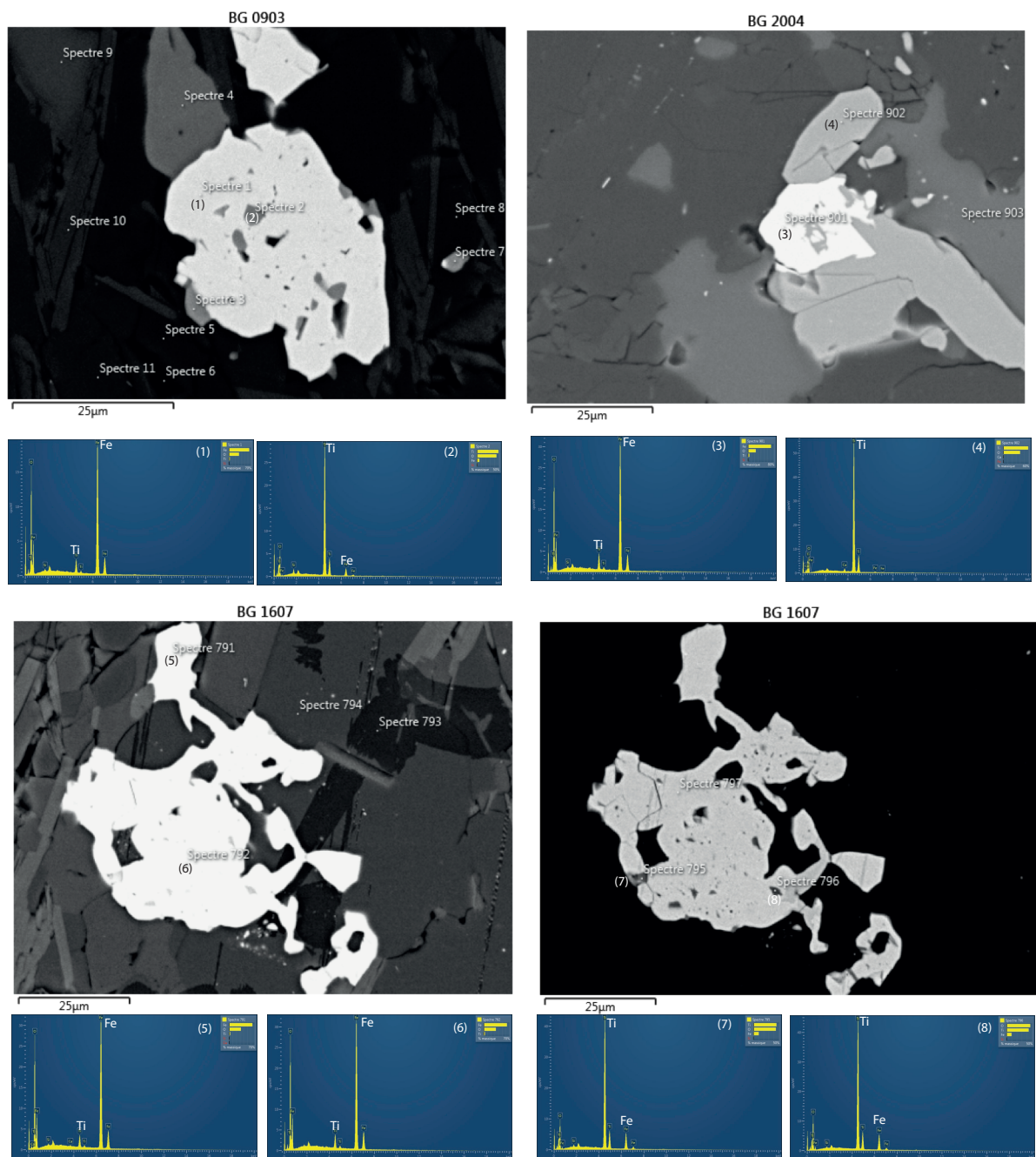


Figure S7. Examples of SEM images of Titanohematite with spots and corresponding EDS spectra.

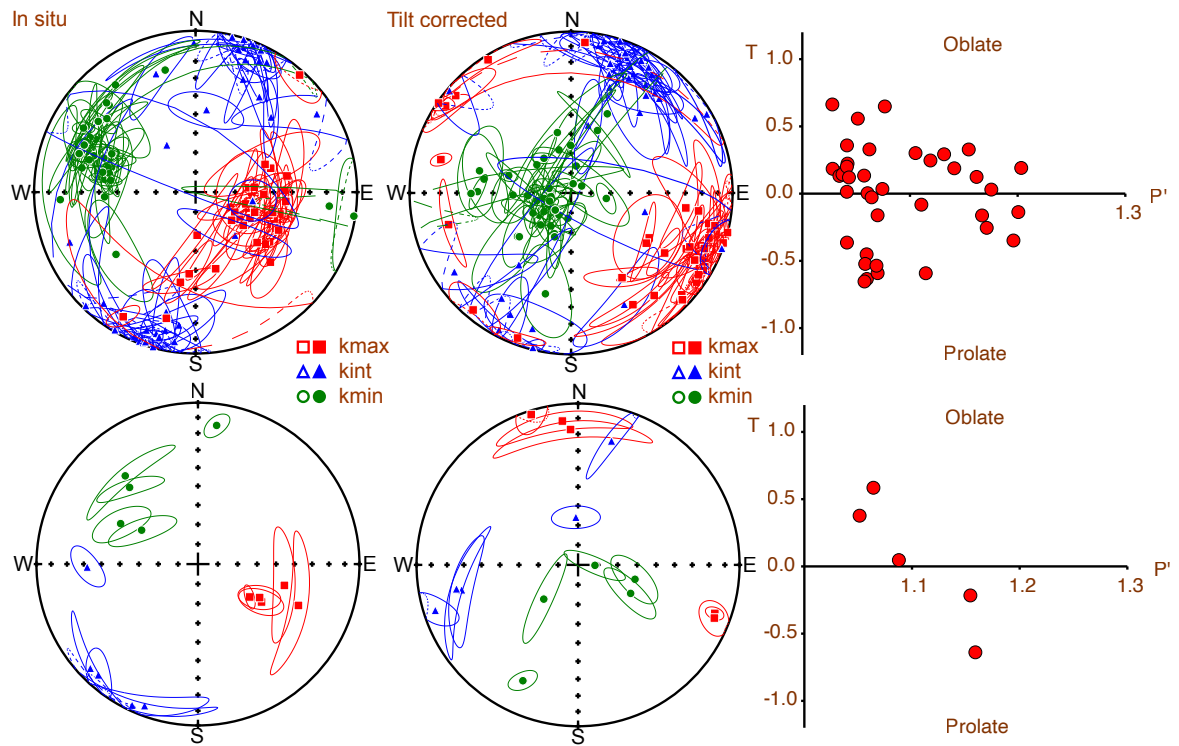


Figure S8. Equal area plots of AMS data at the site level in in situ (left) and tilt corrected coordinates (center) for all sites from the NW limb of the syncline (top) and sites from the SE overturned limb of the syncline (bottom). Left) T-P' plot showing the shape parameter of the ellipsoid versus the corrected degree of anisotropy P' .

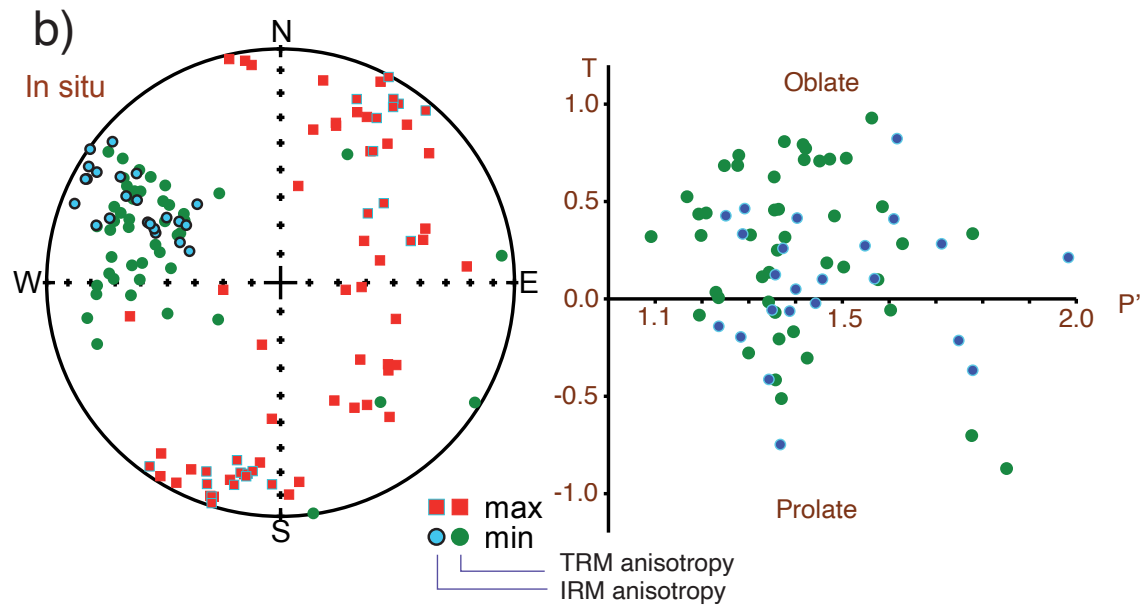


Figure S9. a) Plot of the main directions of ellipsoids on anisotropy of remanent magnetization either IRM at 950 mT or low field (50 μ T) thermoremanent magnetization (TRM). b) Plot of the parameter T defining the shape of the ellipsoids versus the corrected degree of anisotropy P'. Blue (green) symbols correspond respectively to IRM (TRM) anisotropy tensors.

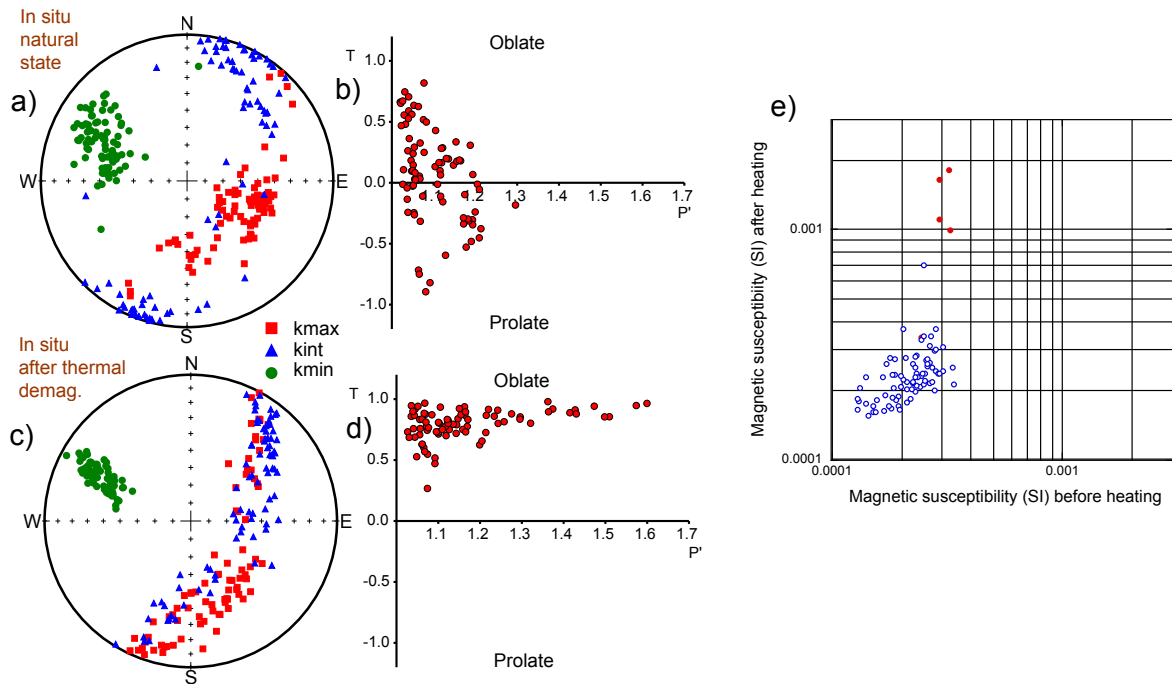


Figure S10. Comparison of the AMS data before (a) and after (b) thermal demagnetization above 600°C for the same set of 83 specimens from various sites in the Bartang volcanoclastic sediments. Equal area plots and T-P' diagram as in Figure S8. C) comparison of the magnetic susceptibility for the AMS data before and after thermal heating. Red dots are from samples of site BG39 for which there is a significant increase in magnetic susceptibility after heating.

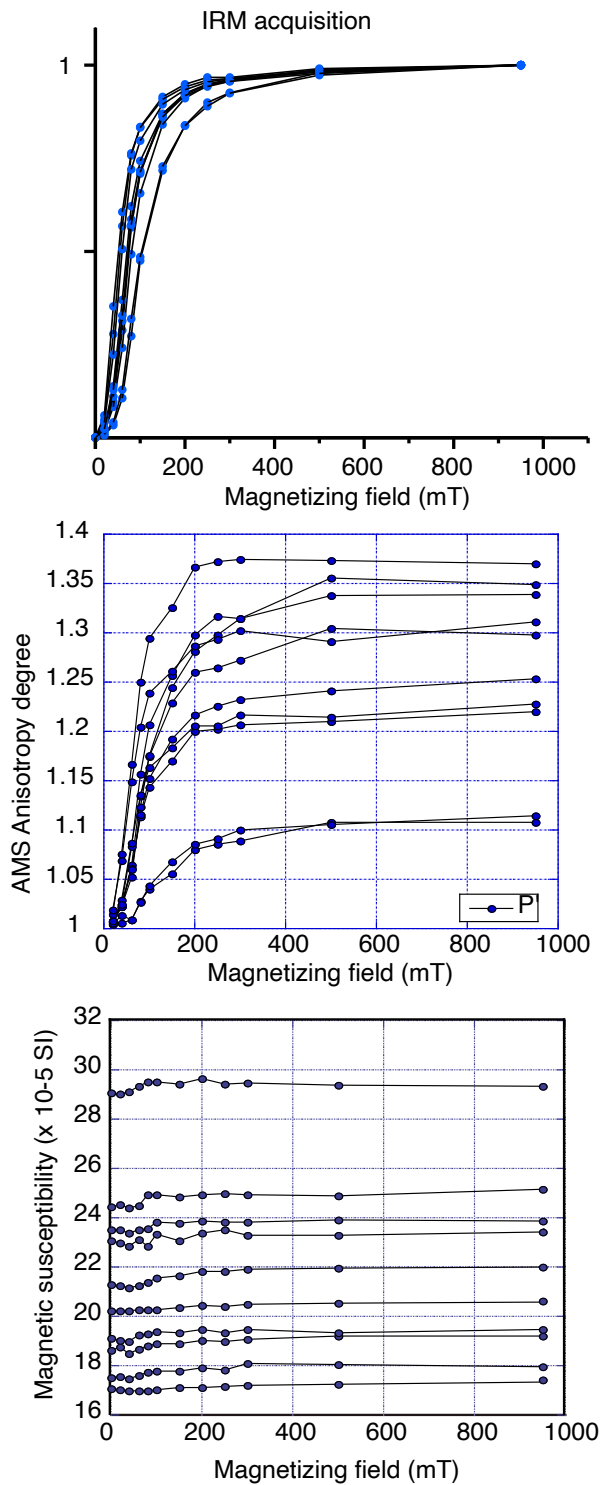


Figure S11. top) XY plot of the normalized IRM acquisition. middle) Plot of the corrected AMS anisotropy degree P' versus the intensity of the field used in IRM acquisition in the Z sample axis. bottom) Plot of the mean tensor magnetic susceptibility value after each step of IRM acquisition.

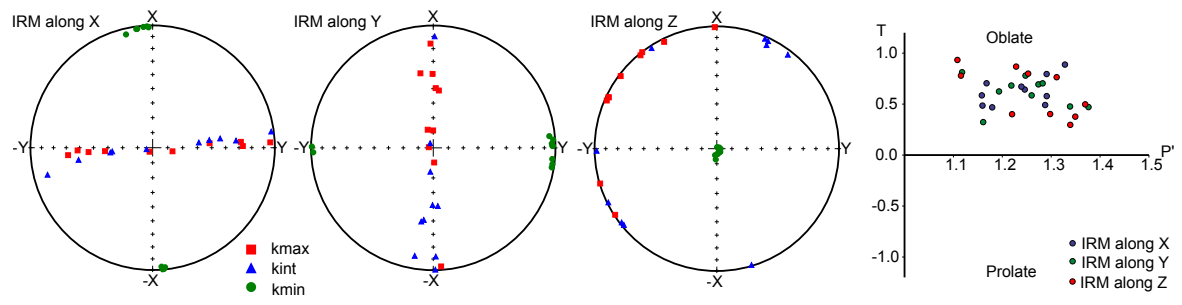


Figure S12. Field impressed AMS after an IRM acquisition along x,y,z. The minimum axis is along the IRM.

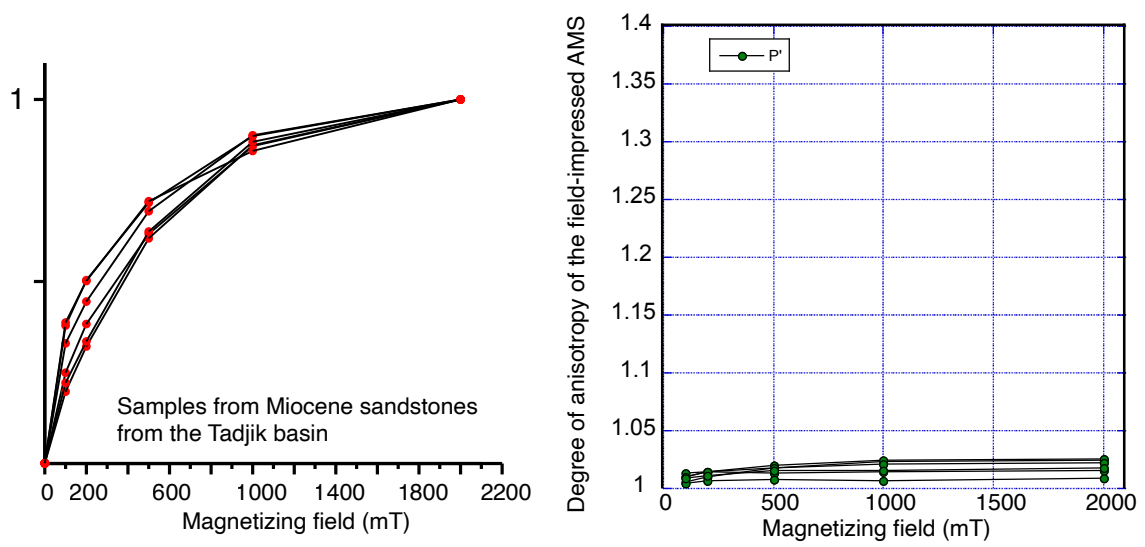


Figure S13. Left) IRM acquisition in samples from Miocene sandstones of the Tadjik basin. Right) degree of anisotropy induced by IRM acquisition.